The Astrophysical Journal Supplement Series, 286:38 (27pp), 2026 September https://doi.org/10.3847/1538-4365/ae9081
© 2026. The Author(s). Published by the American Astronomical Society.
OPEN ACCESS

Investigating the Young Stellar Populations and Hierarchies in Nearby Galaxies with the UVIT. II. Presenting the Properties of ∼25,000 UV-detected Star-forming Clumps

Gairola Shashank[1,2], Smitha Subramanian[1,2,3], Chayan Mondal[4,5], Shyam H. Menon[6,7], and Annapurni Subramaniam[1]
[1] Indian Institute of Astrophysics, Koramangala II Block, Bangalore-560034, India; shashank.gairola@iiap.res.in, shashankgairola17@gmail.com
[2] Pondicherry University, R.V. Nagar, Kalapet, 605014, Puducherry, India
[3] Leibniz-Institut für Astrophysik Potsdam, An der Sternwarte 16, D-14482 Potsdam, Germany
[4] S. N. Bose National Centre for Basic Sciences Block-JD, Sector-III, Salt Lake, Kolkata-700106, India
[5] Academia Sinica Institute of Astronomy and Astrophysics (ASIAA), No. 1, Section 4, Roosevelt Road, Taipei 10617, Taiwan
[6] Center for Computational Astrophysics, Flatiron Institute, 162 5th Avenue, New York, NY 10010, USA
[7] Department of Physics and Astronomy, Rutgers University, 136 Frelinghuysen Road, Piscataway, NJ 08854, USA
Received 2026 January 28; revised 2026 June 10; accepted 2026 July 7; published 2026 September 10

Abstract

Studying young stellar populations within galaxies can help refine our understanding of recent star formation in galaxies and their evolution. With this motivation, we present a catalog of ∼25,000 recently formed (within 400 Myr) star-forming clumps (SFCs) in 17 morphologically diverse nearby galaxies, including 8 massive, classic spirals, 6 intermediate-mass, flocculent spirals, and 3 dwarf irregulars. We used far- (FUV) and near-UV observations from the Ultraviolet Imaging Telescope, whose ∼1.″5 angular resolution and 28′ field of view allow us to probe SFCs at a mean physical scale of ∼54 pc, within the full extent of our galaxies. We adopted a homogeneous SFC detection criterion, corrected for spatially varying dust attenuation (using 6″ resolution A_V maps, made by combining FUV with archival infrared observations), and estimated the SFC ages by comparing the observed UV color–magnitude diagrams with Starburst99 simple stellar population models. Using our SFC catalog, we studied the age demographic of the recently formed stellar populations across different galaxy morphologies and observed age trends consistent with several well-known phenomena, such as the inside-out formation of disk galaxies, local gravitational instabilities leading to flocculent spiral arms, and the stochastic nature of star formation in dwarf galaxies. Leveraging full galaxy coverage and FUV data, our catalog complements existing optically identified star cluster catalogs in the literature toward improving our understanding of star formation across a wide range of galaxy morphologies, masses, and environments. We make the SFC catalog and A_V maps of our 17 galaxies publicly available with this paper.

Unified Astronomy Thesaurus concepts: Star formation (1569); Galaxies (573); Stellar populations (1622); Ultraviolet astronomy (1736)

Materials only available in the online version of record: machine-readable tables

1. Introduction

Galaxies, giant agglomerations of stars, gas, dust, and dark matter, come in different masses, sizes, star formation rates (SFRs), colors, and morphologies (E. P. Hubble 1936; G. de Vaucouleurs et al. 1991; R. J. Buta et al. 2007; S. Salim et al. 2007). They are the unitary building blocks of the Universe, so it is important to understand how galaxies assemble their baryonic components and evolve over many Gyr of their lifetimes, often transitioning across morphologies. Star formation is one of the important processes that governs galaxy growth and evolution. In galaxies of different masses and morphologies, the star formation process is influenced by a wide variety of common or mutually exclusive physical processes such as gas accretion, dynamical shocks, local or global instabilities, feedback, and galaxy interactions (J. Kormendy & R. C. Kennicutt 2004; J. J. Lemonias et al. 2011; J. Kormendy 2013; S. H. Ho et al. 2019; M. R. Krumholz et al. 2019). Given the context, nearby galaxies serve as ideal testing grounds for theories of star formation and galaxy evolution. Due to their proximity, high-resolution multiwavelength observations of nearby galaxies can be used to study them in great detail, from individual stars to star clusters to any larger stellar structures. By analyzing the spatial distribution of different stellar populations in nearby galaxies, we can better understand how different internal or external processes affect the assembly and evolution of galaxies.

Many studies have leveraged the ultraviolet (UV) emission arising from young, massive stars to characterize the recently formed (within the past ∼400 Myr) stellar populations in nearby galaxies. On one hand, far- and near-UV (FUV and NUV) observations from Galaxy Evolution Explorer (GALEX) have been used to address topics such as the inside-out growth of galaxies, identification and characterization of extended-UV disk galaxies and the spatial distribution of stellar populations (D. A. Thilker et al. 2005a, 2005b, 2007; A. Gil de Paz et al. 2007; J. C. Muñoz-Mateos et al. 2007; J. J. Lemonias et al. 2011). GALEX's 1.°5 diameter field of view (FoV) allows the probing of complete star-forming disks of nearby galaxies, but its coarse ∼6″ angular resolution tends to miss out on the details of star formation on smaller scales, where interesting gas, dust, and feedback physics is involved. On the other hand, studies using the Hubble Space Telescope (HST) have probed star-forming regions at an incredibly high, ∼0.″1 angular resolution with multiband NUV and optical

Original content from this work may be used under the terms of the Creative Commons Attribution 4.0 licence. Any further distribution of this work must maintain attribution to the author(s) and the title of the work, journal citation and DOI.

observations. Legacy ExtraGalactic Ultraviolet Survey (LEGUS) and Physics and High ANGular resolution in Nearby Galaxies Survey (PHANGS) have produced extensive HST-based star cluster catalogs (with ages between 1 Myr and few Gyr) (D. Calzetti et al. 2015; A. Adamo et al. 2017; D. O. Cook et al. 2019; J. C. Lee et al. 2022; D. Maschmann et al. 2024; D. A. Thilker et al. 2025). In conjunction with these star cluster catalogs, HST data have brought insights into stellar population modeling, star cluster evolution, hierarchical star formation, stellar feedback, and the association of spiral arms with star formation (D. J. Radburn-Smith et al. 2012; F. Shabani et al. 2018; E. Sacchi et al. 2019; M. J. Rodríguez et al. 2020; S. H. Menon et al. 2021; S. T. Linden et al. 2022; B. Meena et al. 2025). However, due to HST's $3' \times 3'$ FoV, often multiple pointings are needed to cover even a single nearby galaxy. Usually, only the inner disk of galaxies is covered in these observations, which leaves the lower-metallicity, low-density outskirts of the galaxies unexplored.

Therefore, the optimization between the angular resolution and FoV that the UltraViolet Imaging Telescope (UVIT; P. C. Agrawal 2006; A. Kumar et al. 2012; K. P. Singh et al. 2014) offers ($\sim$1.5″ angular resolution, 28′ diameter FoV) is a valuable asset that can be utilized to better understand the recent star formation activity in galaxies. UVIT has $\sim$4 times better angular resolution than GALEX (UVIT's angular resolution corresponds to $\sim$73 pc at 10 Mpc distance), and it offers a significant FoV advantage over the HST. Moreover, UVIT's FUV coverage offers greater sensitivity in detecting the youngest stellar populations in galaxies as compared to the NUV filter (the bluest available wave band) used in the HST-based studies. Several studies in the past have leveraged these features of the UVIT to study different aspects of extragalactic star formation (K. George et al. 2018; C. Mondal et al. 2018, 2021; J. Yadav et al. 2021; K. Ujjwal et al. 2022; R. Rakhi et al. 2023; S. Amrutha et al. 2024; H. Hassani et al. 2024; S. Hota et al. 2024a, 2024b; C. Watts et al. 2024; K. R. Akhil et al. 2025; R. Chauhan et al. 2025; S. Keshri et al. 2025; G. Santhosh et al. 2025; S. Ananthu et al. 2026). These studies used diverse source detection techniques and dust attenuation correction methods as per the requirements of their science goals. However, most of these studies either focus on a small sample of galaxies or focus on galaxies of a specific morphology. Thus, systematic UVIT-based studies for a large galaxy sample, spanning a wide range in mass and morphology, are rare. Ideally, such studies should characterize stellar populations in different galaxies with a homogeneous methodology and carefully account for the spatially varying internal dust attenuation (C.-N. Hao et al. 2011; M. Boquien et al. 2016; D. Calzetti et al. 2025).

It is against this background that we utilized UVIT observations of 17 nearby (distance $<$20 Mpc), morphologically diverse sample of galaxies to construct an extensive catalog of $\sim$25,000 recently formed (within 400 Myr), UV-detected star-forming clumps (SFCs). Facilitated by the UVIT's 28′ FoV, we covered all the 17 galaxies fully at $\lesssim$1.″5 angular resolution, adopted a homogeneous SFC detection and characterization approach (see Section 3), and took into account spatially variable internal dust attenuation. Framed in the context of past surveys and studies, our catalog offers the following key advancements: (1) Compared to the past surveys (e.g., the LEGUS and PHANGS surveys), which primarily targeted massive, star-forming main-sequence spiral galaxies, our sample includes many intermediate- and low-mass galaxies, with flocculent spiral structure or irregular morphology. This has allowed us to study star formation in a representative sample of morphologically diverse, nearby galaxies. These high-resolution multiwavelength studies (LEGUS/PHANGS) covered a few tens of percent of galaxy area, mostly located in the inner regions of galaxies, whereas our FoV advantage enables full galaxy coverage. This is advantageous for galaxies of large angular size ($>$20′), such as NGC 5457, NGC 300, and NGC 2403, which would have required multiple pointings with the HST/JWST-based studies. This enabled us to study the full star-forming extent of galaxies, including the low-density outer regions, which provide intriguing environments for star formation studies, owing to their low stellar surface density, metal- and dust-poor nature, and abundance of H I (D. A. Thilker et al. 2007; J. Yadav et al. 2021). Furthermore, UVIT FUV observations allow the detection and characterization of the youngest star-forming regions, unlike the NUV- or *V*-band-based detection method used in LEGUS. (2) Compared to GALEX-based studies, our catalog has 3–4 times better spatial resolution. (3) Relative to our past UVIT study (G. Shashank et al. 2025, Paper I from here on), we have now added 13 more galaxies to our sample, nearly quadrupling its size. Moreover, the spatially resolved attenuation correction represents a significant improvement, and the discussion of the age demographics is a major highlight (see Section 4). (4) Finally, with our homogeneous analysis method and spatially varying attenuation correction, our catalog attempts to bridge the gap left by the plethora of past UVIT-based studies of star formation in nearby galaxies.

This SFC catalog can be used to study different topics, such as the galaxy assembly process, secular or interaction-driven star formation and galaxy evolution, hierarchical star formation, and the UV luminosity function of star-forming regions in galaxies. This catalog can also be combined with kinematic data in the future to understand the symbiotic interplay between galactic dynamics and star formation. In this paper, we have utilized this catalog to investigate the recently formed stellar population demographic in galaxies of different morphologies. In our forthcoming paper (G. Shashank et al. 2026, in preparation, henceforth Paper III; the current paper is Paper II), we will use our catalog to explore hierarchical star formation in these 17 galaxies. Recent studies suggest that the hierarchical star formation process occurring within galaxies exhibits a dependence on large-scale galaxy properties (D. M. Elmegreen et al. 2014; K. Grasha et al. 2017; M. J. Rodríguez et al. 2020; S. H. Menon et al. 2021). In Paper I, we investigated this dependence in four spiral galaxies and demonstrated UVIT's capabilities in effectively probing hierarchical star formation in nearby galaxies, on scales between a few parsecs up to several kiloparsecs. Paper III will expand our investigation of hierarchical star formation to a larger sample of 17 galaxies, spanning a broader parameter space in stellar mass and morphology.

The remaining paper is structured as follows. In Section 2, we describe our galaxy sample, along with the observational data we have used. Section 3 describes the various methods involved in the preparation of the extensive SFC catalog in our sample galaxies. In Section 4, we present a discussion of the age demographics of SFCs characterized within our galaxies,

and finally, in Section 5, we summarize our key findings and also outline our future goals.

2. Data

2.1. A Morphologically Diverse Galaxy Sample

For this study, we compiled a UVIT-based, morphologically diverse sample of 17 star-forming galaxies so as to include grand design spirals, flocculent spirals, and dwarf irregulars, all located within a distance of 20 Mpc (see Table 1 for distances and Figure 1 for the UVIT images of the galaxies). The mean galaxy distance for our sample is ∼7.4 Mpc, which translates to a reasonably good spatial resolution of ∼54 pc. We used the stellar mass, visual inspection of the spiral structure, and the literature-based classifications to divide our galaxy sample into three categories as follows. Our galaxy sample includes three dwarf irregulars (dIrr) with no prominent spiral structure, each having mass less than $10^9\,M_\odot$; six intermediate-mass, flocculent spirals with fragmented spiral structure, each having mass ranging from $\sim 10^9$ to $10^{10}\,M_\odot$; and eight massive, classic spirals with well-defined spiral structure, each having mass greater than $10^{10}\,M_\odot$. Among the galaxies in our sample, the dIrr galaxy Wolf–Lundmark–Melotte (WLM) has the lowest stellar mass ($M_* = 4.3 \times 10^7 M_\odot$), while the massive classic spiral NGC 1512 is the most massive ($M_* = 5.2 \times 10^{10} M_\odot$. The physical characteristics of our sample galaxies are provided in Table 1.

These galaxies were selected based on the availability of archival, UVIT FUV, and NUV observations, as the FUV −NUV color of the SFCs is crucial for our age-estimation method. To correct for dust attenuation in a spatially resolved manner, we used the method presented by M. Boquien et al. (2016), which requires near-infrared (NIR) and mid-infrared (MIR) observations (see Section 3.4 for dust attenuation correction). We took the Two Micron All-Sky Survey (2MASS) *J*-band images from T. H. Jarrett et al. (2003) as our NIR data and Multiband Imaging Photometer for Spitzer (MIPS) 24 μm images from D. A. Dale et al. (2009) as our MIR data. Ultimately, the availability of the aforementioned FUV, NUV, NIR, and MIR data dictated the final number of 17 galaxies studied in this paper.

2.2. Observational Data

2.2.1. UV Imaging Data and Reduction

We used archival FUV and NUV observations, taken with the 37.5 cm aperture, UVIT telescope, which is one of the five science instruments on board the AstroSat satellite, operating in a low Earth orbit (P. C. Agrawal 2006; A. Kumar et al. 2012; K. P. Singh et al. 2014). UVIT is a twin telescope with simultaneous imaging capability in FUV (1200–1800 Å), NUV (1800–3200 Å), and visible (VIS; 3200–5500 Å) wave bands. VIS observations are not used for science purposes and are only used in the drift correction process (which corrects for the movement of the telescope's pointing between orbits of observation). UVIT offers angular resolutions better than 1.5″ in both FUV and NUV, and it has a suite of FUV and NUV filters, with varying central wavelengths and bandwidths.

We downloaded the level 1 data from the AstroSat archive and reduced it using the dedicated UVIT data reduction software CCDLAB (J. E. Postma & D. Leahy 2017).

The detailed data reduction process to create the final UVIT science-ready images is described in Section 2 of Paper I. It involves multiple steps, such as drift correction, flat-fielding, aligning and merging observations taken in different orbits, point-spread function (PSF) optimization, and establishing the world coordinate system in the images. Small differences in the accuracy with which these steps can be performed in CCDLAB affects the final PSF of the science-ready images (J. E. Postma & D. Leahy 2017). This means that our UVIT images of 17 galaxies have PSF FWHM values ranging from 1.1″ to 1.5″ (see Table 1). In order to maximize the exposure times of our FUV and NUV images, we also merged multiepoch observations for some of the galaxies, taken by different observing proposals. We make the science-ready FUV and NUV images of our sample galaxies publicly available via Zenodo at doi:10.5281/zenodo.21319450. The details of all the UVIT data used in this work and the total exposure times are summarized in Table 2.

2.2.2. Near- and Mid-infrared (MIR and NIR) Data

To correct for dust attenuation (see Section 3.4), we used the archival NIR and MIR data. For NIR, we used archival J-band data from 2MASS (T. H. Jarrett et al. 2003). 2MASS was an all-sky NIR survey offering angular resolutions of ∼2″ in the *J* band (1.2 μm). In T. H. Jarrett et al. (2003), the global NIR properties along with the *J*-, *H*- and *K*-band images of the 100 brightest galaxies covered by 2MASS were presented. For MIR, we used archival MIPS 24 μm data from the Spitzer Infrared Nearby Galaxies Survey (SINGS) (R. C. Kennicutt et al. 2003; D. A. Dale et al. 2009). There are 75 galaxies in the SINGS survey, imaged at ∼6″ angular resolution. The aim of the SINGS survey was to characterize the IR emission of galaxies across a broad range of galaxy properties and star formation environments. We obtained the science-ready NIR and MIR images directly from the NASA Extragalactic Database (NED)[8] for our analysis.

3. SFC Catalog Preparation

The age demographics of different stellar populations within galaxies can help us better understand the physical processes responsible for shaping the structure of galaxies. For this purpose, full galaxy coverage age maps of stellar populations are essential, which motivated us to create this catalog, consisting of ∼25,000 SFCs. Through UV selection, we are only probing the stellar populations formed within the past 400 Myr in these galaxies, which convey the picture of the recent star formation and galaxy assembly process.

This paper is the second in a series of papers, following up on G. Shashank et al. (2025) (Paper I), investigating hierarchical star formation in a statistically large sample of nearby galaxies using a homogeneous methodology. Most of the methods used in the current paper related to SFC characterization are the same as in Paper I. We provide a complete description of our methodology here. However, we refer interested readers to Paper I for a more nuanced description and clear motivations for the choices made in this paper. Each successive paper in this series differs from its predecessors, as we try to implement more science and a larger

[8] http://ned.ipac.caltech.edu

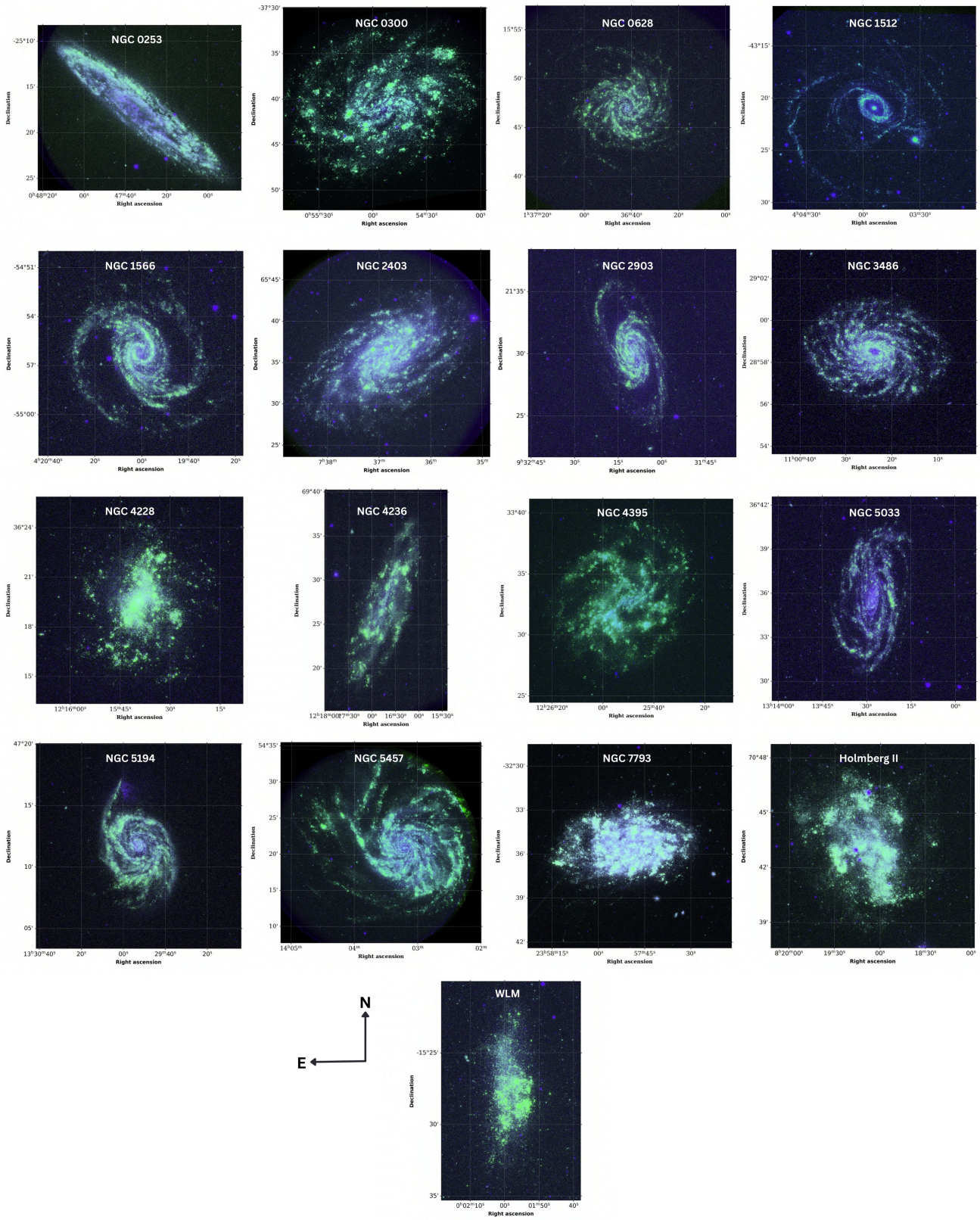


Figure 1. Color-composite images of the 17 galaxies studied in this paper. Color scheme chosen to generate these images: red = (FUV + NUV)/2, green = FUV × 1.5, and blue = NUV × 1.5.

number of galaxies into our investigation. For example, NGC 1566, NGC 5194, NGC 5457, and NGC 7793 were also part of Paper I. But in Paper I, we could not take into account spatially variable dust attenuation and instead used galaxy-averaged attenuation correction. This warrants the inclusion of these four galaxies in the galaxy sample selected for this paper.

Table 1
Some Important Properties of the Selected Galaxies in This Study

Galaxy	R.A.	Decl.	Morphological Subclass	P.A.	Incl.	Distance	Stellar Mass	UVIT PSF FWHM	Spatial Resolution
	(deg)	(deg)		(deg)	(deg)	(Mpc)	($M_{\odot}$)	(arcsec)	(pc)
(1)	(2)	(3)	(4)	(5)	(6)	(7)	(8)	(9)	(10)
NGC 0253	11.8880	−25.2880	Massive, classic spiral	52.5 (a)	75.0 (a)	3.7 (a)	5.0×10^{10} (a)	1.5	27
NGC 0300	13.7227	−37.6842	Intermediate-mass floccu-lent spiral	114.3 (a)	39.8 (a)	2.1 (a)	1.5×10^{9} (a)	1.3	12
NGC 0628	24.1741	+15.7837	Massive, classic spiral	20.7 (b)	8.9 (b)	9.8 (b)	1.1×10^{10} (b)	1.5	71
NGC 1512	60.9757	−43.3488	Massive, classic spiral	261.9 (c)	42.5 (c)	18.8 (c)	5.2×10^{10} (c)	1.5	137
NGC 1566	65.0016	−54.9379	Massive, classic spiral	214.7 (b)	29.6 (b)	17.7 (b)	2.7×10^{10} (b)	1.2	103
NGC 2403	114.2137	+65.6027	Intermediate-mass floccu-lent spiral	124.0 (d)	63.0 (d)	3.2 (d)	5.0×10^{9} (d)	1.3	19
NGC 2903	143.0421	+21.5008	Massive, classic spiral	203.7 (c)	66.8 (c)	10.0 (c)	4.4×10^{10} (c)	1.1	50
NGC 3486	165.0996	+28.9751	Intermediate-mass floccu-lent spiral	80.0 (e)	50.0 (e)	11.4 (f)	6.3×10^{9} (g)	1.5	83
NGC 4228	183.9132	+36.3268	Dwarf irregular	65.0 (d)	44.0 (d)	2.9 (d)	6.3×10^{8} (d)	1.4	20
NGC 4236	184.1755	+69.4626	Intermediate-mass floccu-lent spiral	162.0 (h)	75.0 (h)	4.5 (h)	9.2×10^{8} (i)	1.2	21
NGC 4395	186.4536	+33.5469	Intermediate-mass floccu-lent spiral	147.0 (j)	38.0 (j)	4.3 (j)	2.5×10^{9} (j)	1.1	23
NGC 5033	198.3645	+36.5939	Massive, classic spiral	352.0 (k)	68.0 (k)	16.5 (k)	3.7×10^{10} (l)	1.5	120
NGC 5194	202.4696	+47.1952	Massive, classic spiral	173.0 (b)	22.0 (b)	8.6 (b)	2.4×10^{10} (b)	1.1	46
NGC 5457	210.8023	+54.3489	Massive, classic spiral	39.0 (b)	18.0 (b)	6.7 (b)	1.9×10^{10} (b)	1.5	49
NGC 7793	359.4572	−32.5910	Intermediate-mass floccu-lent spiral	98.0 (b)	55.0 (b)	3.6 (b)	3.2×10^{9} (b)	1.4	24
Holmberg II	124.7701	+70.7199	Dwarf irregular	177.0 (d)	41.0 (d)	3.4 (d)	2.0×10^{9} (d)	1.3	21
WLM	0.4924	−15.4611	Dwarf irregular	181.0 (m)	69.0 (m)	1.0 (m)	4.3×10^{7} (n)	1.4	6

Note. (1) Galaxy name, (2) R.A., (3) decl., (4) morphological classification (described in Section 2.1), (5) position angle, (6) inclination angle, (7) distance, (8) stellar mass, (9) UVIT point-spread function (PSF) full width at half maximum (FWHM), and (10) corresponding spatial resolution for each of our sample galaxies, respectively.

References. (a) H. Hassani et al. (2024); (b) S. H. Menon et al. (2021); (c) A. K. Leroy et al. (2021); (d) A. K. Leroy et al. (2008); (e) Z.-M. Zhou et al. (2015); (f) NED; (g) M. V. Smith et al. (2022); (h) K. T. Chyży et al. (2007); (i) L. K. Hunt et al. (2019); (j) P. Nandi et al. (2023); (k) A. H. C. Thean et al. (1997); (l) F. Bresolin (2019); (m) C. Mondal et al. (2018); (n) Y. Zheng et al. (2019).

3.1. Identification of SFCs from the FUV Data

UV emission arising from galaxies is a direct tracer of recent star formation, and FUV emission traces the youngest stellar populations much more effectively as compared to NUV (A. Gil de Paz et al. 2007; D. A. Thilker et al. 2007; C. Mondal et al. 2018, 2021; J. Yadav et al. 2021; K. Ujjwal et al. 2022; S. Amrutha et al. 2024; S. Subramanian et al. 2024; C. Watts et al. 2024; R. Chauhan et al. 2025). So, in order to detect the SFCs in our sample galaxies, we applied the Astrodendro source detection algorithm to their FUV images. Astrodendro was developed to explore the hierarchical distribution of flux in astronomical images (E. W. Rosolowsky et al. 2008). It establishes hierarchical connections between different regions in the two-dimensional (2D) flux maps (in the form of a dendrogram tree) by scanning from the peak flux point to the minimum flux floor. It classifies different flux regions into trunks, branches, and leaves—in increasing order of flux density and decreasing order of compactness. Leaves are the structures of the most interest to us, as these are the smallest structures that are identifiable in a given flux map by Astrodendro and cannot be divided any further. For this reason, Astrodendro leaves are used as SFCs in our study.

Astrodendro uses three input parameters: (1) min_value, which we set equal to three times the standard deviation (σ) of the sky background plus one times the sky background (bg), serves as the detection threshold below which no structures should be identified; (2) min_delta, which we set equal to one times the standard deviation (σ), is used as a deblending criterion to create segmentation between two closely located SFCs; and (3) min_npix, which we set equal to 11 pixels (equivalent to a circular PSF of 1.5″ diameter FWHM), corresponds to the angular resolution of the UVIT, in pixel units. Both min_value and min_delta values are defined per pixel, and all the leaf structures identified by the Astrodendro are a collection of contiguous pixels. In Appendix A, we present a sensitivity analysis that demonstrates that the number of detected SFCs and our scientific results are robust against the variation in astrodendro input parameters, at least by a factor of 2. We used the indices, positions, and sizes of the leaf structures identified by Astrodendro in our subsequent analysis.

3.2. Estimation of SFC Ages

Several studies in the literature have demonstrated that dust attenuation corrected UV color of a star-forming region can serve as an indicator of its age (L. Bianchi et al. 2005; D. A. Thilker et al. 2005a, 2005b; J. C. Muñoz-Mateos et al. 2007; C. Mondal et al. 2021; K. Ujjwal et al. 2022). So, we estimated ages of the detected SFCs by comparing their observed, attenuation-corrected FUV−NUV color versus FUV magnitude color–magnitude diagram (termed UV CMD from here on) against the synthetic UV CMDs generated using

Table 2
Description of the UVIT Observations of the Sample Galaxies and the Number of SFCs Identified in Each Galaxy

Galaxy	FUV Filter	FUV Exposure (ks)	NUV Filter	NUV Exposure (ks)	R_{FUV}	R_{NUV}	Mag. Error	N_{SFC}	Completeness Magnitude (mag)	Completeness Age (Myr)	Age Remark
(1)	(2)	(3)	(4)	(5)	(6)	(7)	(8)	(9)	(10)	(11)	(12)
N0253	F169M	11.29	N245M	11.98	2.55	2.43	0.10	1348	20.00	25	UL
N0300	F148W	8.07	N242W	11.71	2.69	2.50	0.10	4947	21.60	210	UL
N0628	F154W	4.42	N263M	1.83	2.61	2.11	0.25	883	20.80	10	OK
N1512	F154W	4.78	N242W	2.80	2.61	2.50	0.20	385	21.90	6	UL
N1566	F148W	2.94	N263M	2.96	2.69	2.11	0.20	1194	21.30	30	OK
N2403	F148W	5.38	N242W	5.99	2.69	2.50	0.10	2144	20.80	60	UL
N2903	F148W	3.35	N263M	3.35	2.69	2.11	0.20	1180	20.70	6	OK
N3486	F148W	1.91	N263M	2.20	2.69	2.11	0.25	864	21.60	15	OK
N4228	F148W	5.70	N219M	2.80	2.69	3.16	0.25	648	21.10	80	UL
N4236	F148W	3.89	N263M	3.79	2.69	2.11	0.20	1194	22.20	100	OK
N4395	F148W	19.02	N263M	1.45	2.69	2.11	0.20	947	21.70	75	OK
N5033	F148W	2.93	N263M	2.95	2.69	2.11	0.25	647	22.30	15	OK
N5194	F148W	1.89	N263M	1.02	2.69	2.11	0.20	1694	20.40	10	OK
N5457	F148W	3.34	N263M	3.28	2.69	2.11	0.10	1507	20.40	14	OK
N7793	F148W	7.57	N242W	8.11	2.69	2.50	0.10	1775	21.20	70	UL
Holmberg II	F154W	18.38	N245M	17.38	2.51	2.43	0.10	1181	22.50	190	UL
WLM	F148W	10.18	N263M	5.25	2.69	2.11	0.20	1357	23.20	>400	OK

Note. (1) Galaxy name, (2) FUV filter, (3) FUV exposure time, (4) NUV filter, (5) exposure time, (6) attenuation coefficient for the FUV and (7) NUV filters derived using Cardelli's law (J. A. Cardelli et al. 1989), (8) finalized FUV and NUV magnitude error cut (refer to Section 3.2), (9) final number of SFCs characterized, (10) completeness limit FUV magnitude, (11) the corresponding age (for an SFC of $10^4\ M_\odot$) (refer to Section 3.6), and (12) remarks about the age estimate (refer to Section 3.5), respectively. Abbreviations: OK = age estimates are reliable, while UL = age estimates may be systematically overestimated and therefore represent upper limits.

Starburst99 (SB99) stellar population synthesis models (C. Leitherer et al. 1999). We have described our dust attenuation correction methodology in Section 3.4. However, throughout this section, it should be assumed that each SFC was corrected for spatially varying dust attenuation.

To produce the observed UV CMD, we estimated the FUV and NUV magnitudes for the SFCs by performing circular aperture photometry on the leaves/SFCs identified by Astrodendro and using the UVIT-specific counts to AB magnitude conversion provided in S. N. Tandon et al. (2020). For a given SFC, the area of the circular aperture is kept equal to the area of the irregularly shaped SFC detected by Astrodendro. We also measured the FUV and NUV magnitude errors associated with each SFC by applying error propagation on the counts to AB magnitude conversion formula, and assuming the error on the observed counts to be Poisson errors. The sky background (bg) contribution was also subtracted during the measurement of FUV and NUV magnitudes. Next, we corrected the observed FUV and NUV magnitudes and FUV−NUV color of the SFCs for dust attenuation using our spatially resolved A_V maps (see Section 3.4 and Figures 3 and 15).

To produce the synthetic SB99 CMD, we generated synthetic spectra for star clusters of varying ages ranging from 1 to 400 Myr, four discrete stellar mass values (10^3, 10^4, 10^5, and $10^6\ M_\odot$) and three metallicity values ($z = 0.02$, 0.008, and 0.004). It was assumed that the stars would follow the Kroupa initial mass function (IMF) (P. Kroupa 2001) and Geneva high-mass-loss-rate stellar evolutionary tracks. A summary of the important input parameters used to generate the SB99 synthetic spectra is provided in Table 3. We note that we chose only one value of metallicity per galaxy, and the choice of metallicity is informed by the past measurements from literature or the stellar mass–metallicity dependence of the star-forming galaxies (C. A. Tremonti et al. 2004). At the same time, we acknowledge that negative radial metallicity gradients exist in galaxies, which may affect our age estimations (see Appendix B for a discussion.) We convolved the SB99 spectra with the UVIT filter transmission curves (S. N. Tandon et al. 2020) to create the synthetic UV CMDs. We show the age evolution of the synthetic SB99 CMD tracks for different star cluster masses in Figure 2. It is evident from the CMD that, in general, the FUV−NUV color of the SFCs becomes redder with increasing age. This color evolution is fast between ages 0–20 Myr, and slows down significantly beyond 20 Myr as the most massive, FUV-emitting stars reach the end of their main-sequence lives. The stellar mass of the synthetic CMD track has no effect on this color–age relationship. Finally, a comparison between the dust-attenuation-corrected observed UV CMD and the synthetic SB99 UV CMD allowed us to interpolate the observed FUV−NUV color against the synthetic SB99 color and estimate the ages of the observed SFCs.

Table 3
Summary of the Key Input Parameters used in the SB99 SSP Models

Parameter	Value
Star formation type	Instantaneous
Initial mass function (IMF)	Kroupa [slope: 1.3, 2.3]
Stellar mass range	0.1, 0.5, 120 $M_\odot$
Clump mass	10^3, 10^4, 10^5, $10^6\ M_\odot$
Metallicity	$Z = 0.004$ (WLM (C. Mondal et al. 2018))
	$Z = 0.008$ (NGC 4228, Holmberg II)
	$Z = 0.008$ (intermediate-mass flocc. spirals)
	$Z = 0.02$ (high-mass classic spirals)
Evolutionary track	Geneva (high mass-loss rate)
Age range	1–400 Myr

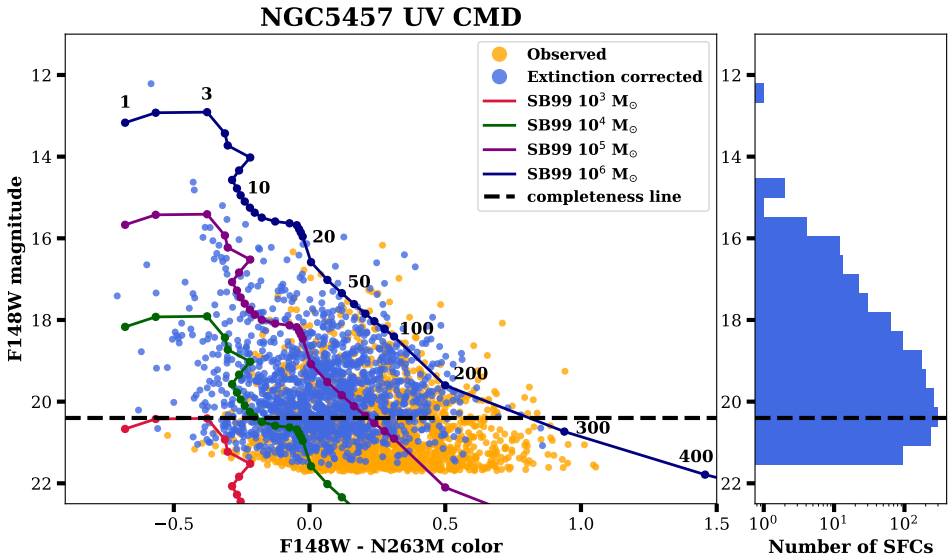


Figure 2. Synthetic Starburst99 vs. observed UV CMD for NGC 5457, which is used for the age estimation of SFCs (refer to Section 3.2). The synthetic colors and magnitudes derived for different ages and masses are represented by the four tracks. The numbers written adjacent to the $10^6\,M_\odot$ track denote the synthetic SFC age in Myr. The observed SFCs with their dust attenuation uncorrected/corrected colors and magnitudes are represented by the orange/blue points. The right-hand side plot shows the FUV magnitude histogram for the SFCs in NGC 5457. The horizontal black dashed line denotes the completeness limits of SFCs, and it corresponds to 20.40 FUV magnitude and ∼14 Myr for an SFC of $10^4\,M_\odot$ (refer to Section 3.6).

In order to estimate the age error associated with a given SFC, we used a pilot approach leveraging the fact that the evolution of FUV−NUV color is quite rapid in the first 20 Myr, slower in 20–100 Myr, and even slower in 100–400 Myr (as can be seen in the UV CMD presented in Figure 2). We assumed that the age and the FUV−NUV color roughly follow linear relationships in these age bins, and therefore we can use error propagation to estimate the age errors. This implies that the error on the SFC age is equal to the product of the error on the observed FUV−NUV color and the slope of the assumed linear relationship between the SFC age and its FUV−NUV color. Here, the slope represents the change in the SFC age corresponding to 1 magnitude change in its FUV−NUV color. We used three different values of this slope in our age error estimation method i.e., slope1 (between 1 and 20 Myr), slope2 (between 20 and 100 Myr), and slope3 (between 100 and 400 Myr). In this paper, we assigned these age errors to the SFCs.

We detected thousands of leaves/SFCs per galaxy in the initial run of Astrodendro on the FUV images. This amounts to a total number much larger than the ∼25,000 SFCs finalized within the 17 galaxies. However, several past studies have utilized magnitude error cuts to reliably constrain the ages of the SFCs (C. Mondal et al. 2018, 2021; K. Ujjwal et al. 2022; Paper I). As the age errors are propagated from the FUV −NUV color errors, which in turn depend on both the FUV and NUV magnitude errors, introducing magnitude error cuts can allow us to keep the age errors to a minimum. Therefore, we started by using the 0.10 mag error cuts for all galaxies. However, in some of our galaxies, we could only detect a few hundred SFCs at the 0.10 mag error limit, owing to their shallow exposure time observations. The aforementioned studies have also shown that a sufficiently large number of SFCs is required in order to investigate the stellar populations demographics in nearby galaxies, which is one of the aims of this paper. Moreover, a sufficiently large number of SFCs within each galaxy (>300–400) will eventually aid our exploration of stellar hierarchies in Paper III. Several studies have shown that, in order to effectively explore stellar hierarchies, a larger number of star-forming regions need to be taken into consideration (K. Grasha et al. 2017; S. H. Menon et al. 2021; B. Meena et al. 2025; G. Shashank et al. 2025). Therefore, we increased the magnitude error cuts to 0.20 and 0.25 mag in some of our galaxies. A summary of the galaxy-specific magnitude error cuts is given in Table 2. We note that the magnitude error cut provided in Table 2 corresponding to any galaxy represents the maximum allowed photometric uncertainty. The actual magnitude errors associated with individual SFCs are smaller than the magnitude error cut and are provided with our SFC catalog presented in Table 6.

We have produced a catalog of approximately 25,000 SFCs in our sample galaxies (see Appendix C for the SFC catalog and Appendix D for the radius distribution of the SFCs within our galaxies). This catalog includes information about the host galaxy name, positions, sizes, FUV and NUV magnitudes, magnitude errors, FUV−NUV color before and after attenuation correction, A_V values, derived ages of all the SFCs, and the associated age errors. Our SFC catalog, along with the complete 6″ resolution dust attenuation maps (Tables 6 and 7 , respectively), is made public with this paper and can be accessed online.

3.3. Nature of SFCs, Resolution Effects, and Implications

The galaxies in our sample lie at distances between 0.9 and 20 Mpc. The UVIT resolution of ∼1.″5 corresponds to a broad range of values, from 6 to 137 pc (see columns 9 and 10 of Table 1), in our galaxies; this spatial scale determines the minimum size of any detected SFC in our galaxies. Owing to this large variation in the physical resolution, the identified SFCs likely correspond to different stellar structures across the sample. For instance, the 6 pc resolution for WLM (the nearest galaxy) is comparable to the typical sizes of massive star clusters. In NGC 7793, the UVIT resolution of 24 pc is equivalent to the sizes of OB associations. Finally, in NGC

1512 (the farthest galaxy), a UVIT resolution of 137 pc corresponds to the sizes of large unbound stellar complexes in spiral galaxies. Apart from WLM, the SFC detection scale for our galaxies is significantly larger than the sizes of single-aged star clusters. Therefore, homogeneously comparing the SFC properties across our galaxy sample should be reasonable.

By overplotting LEGUS star clusters on our SFCs, we observed that many SFCs represent locations where multiple star clusters are clustered together. This implies that modeling the SFCs as single-aged simple stellar populations (SSPs) may not be strictly applicable. The derived age of an SFC encompassing multiple star clusters should represent some form of an average of the ages of its constituting clusters, or the derived SFC age may be older than the average, due to the contamination from older stars in the galactic disk. Our choice of an instantaneous burst of star formation in estimating the SFC ages is perhaps oversimplified, as these SFCs could be forming stars continuously, over many Myr. Ideally, these SFCs should be modeled as composite stellar populations with complex, continuous star formation histories (SFHs). Instantaneous and continuous star formation represent two extreme cases of modeling stellar populations, providing lower and upper limits on ages, respectively. Adopting a continuous star formation model would shift the SFC of a given FUV−NUV color toward older ages, owing to the larger star formation timescale (C. Leitherer et al. 1999; E. M. Levesque & C. Leitherer 2013). In our tests, we find that, although this age shift is observed for both young (1–20 Myr) and old (>20 Myr) SFCs, it is significantly greater for redder/older SFCs.

However, several studies in the past have modeled GALEX/UVIT-detected UV-bright star-forming complexes as well as LEGUS-based OB associations as SSPs, born in instantaneous bursts (J. Iglesias-Paramo et al. 2004; L. Bianchi et al. 2005; D. A. Thilker et al. 2005a; J. C. Muñoz-Mateos et al. 2007; A. Pasquali et al. 2008; A. Adamo et al. 2017; D. O. Cook et al. 2019). As we are detecting SFCs in FUV, using UV color for age determination, and using the instantaneous burst model in this paper, the derived SFC ages may be lower limits. Since the main aim of this paper is to construct an SFC catalog to understand the hierarchical nature of star formation (in Paper III), which evolves with age and disperses within tens of Myr, the lower limits of ages given by the instantaneous burst are more suitable. Our derived ages may not be equivalent to the star cluster ages derived in LEGUS/PHANGS, but may reflect ages of stellar associations in these surveys. Overall, using a continuous SFH instead of an instantaneous SFH would lead to older ages at a given FUV–NUV color value. However, because the shift toward older ages between the instantaneous and continuous SFH is systematic in nature, our conclusions regarding the overall age demographics and age gradients are unlikely to be significantly affected.

3.4. Dust Attenuation Correction

Starlight from external galaxies is attenuated by the dust present along the line of sight, across the UV, optical, and IR wavelengths, with the strongest attenuation in the UV. This attenuation has two contributing components: (1) one due to the Milky Way (MW/foreground) dust and (2) another due to the dust present within the host galaxy itself (internal). The latter component is usually much more dominant than the foreground component. We corrected for the MW/foreground dust toward our sample galaxies using the dust reddening maps accessed from the NASA dust and reddening calculator (E. F. Schlafly & D. P. Finkbeiner 2011). In Paper I, we used a literature-based, galaxy-averaged value of internal dust attenuation correction for all the SFCs within the four sample galaxies. However, dust attenuation in galaxies is spatially variable and not constant, so in this paper, we aimed to correct for internal dust attenuation in a spatially resolved manner. However, the spatially resolved internal dust attenuation maps of our sample galaxies, which have complete galaxy coverage, were not available, which motivated us to create our own attenuation maps.

One of the most widely used methods to correct for dust attenuation in UV consists of combining the UV with the emission from the dust itself (in the infrared (IR) wavelengths). This is based on the fact that UV photons emitted by stars are often absorbed by dust, which in turn raises the dust temperature. This heated dust then emits the reprocessed radiation in IR wavelengths. Past studies based on multi-wavelength (UV, optical, and IR) observations of nearby galaxies have produced empirical calibrations to determine the fraction of IR flux corresponding to dust reprocessed UV emission—parameterized by the IR scaling coefficients (k_i) for UV obscuration (D. Burgarella et al. 2005; V. Buat et al. 2005; D. Calzetti et al. 2007; L. Cortese et al. 2008; C.-N. Hao et al. 2011; D. Calzetti et al. 2025). These calibrations, with a form of Equation (1), can be used to retrieve the true UV flux ($\mathrm{FUV_{total}}$) arising from a star-forming region by combining the observed star-produced UV fluxes ($\mathrm{FUV_{obs}}$) with the dust-produced IR fluxes ($24\mu_{\mathrm{obs}}$, in our case, which corresponds to the heated dust emission in MIPS 24 μm wave band):

$$\mathrm{FUV_{total}} = \mathrm{FUV_{obs}} + k_{24\mu} * 24\mu_{\mathrm{obs}}. \quad (1)$$

The value of k_i ($k_{24\mu}$, in our case) reported in the literature varies, depending on whether the IR emission of heated dust that is not related to recent star formation has been subtracted (a constant value of $k_{24\mu} = 6$ from the study of G. Liu et al. 2011) or not (a constant value of $k_{24\mu} = 3.89$ from the study of C.-N. Hao et al. 2011). It is now well-known that a significant fraction of IR emission arising from heated dust is caused by old stellar populations (M. Sauvage & T. X. Thuan 1992; M. Boquien et al. 2016).

Based on the spectral energy distribution (SED) fitting of spatially resolved regions, M. Boquien et al. (2016) (MB16 from here on) found that k_i varies within galaxies and also varies from galaxy to galaxy. This variation is a function of the relative contribution of young and old stellar populations toward dust heating. MB16 observed that k_i shares a strong linear correlation with star formation history or specific SFR, which can observationally be probed with FUV−NIR color. This allowed them to calibrate k_i using the FUV−NIR color, which is an observable quantity. In this work, we used this calibration relation (as given below) to estimate $k_{24\mu}$ in a spatially resolved manner and use it to find the dust attenuation corrected UV emission:

$$k_{24\mu} = a + b * (\mathrm{FUV_{AB}} - \mathrm{NIR_{AB}}). \quad (2)$$

Here, $\mathrm{FUV_{AB}}$ and $\mathrm{NIR_{AB}}$ are the AB magnitudes in FUV and NIR wavelengths, while a and b are calibration coefficients. We used UVIT FUV, 2MASS J-band (for NIR), and MIPS 24 μm (for FIR) data and adopted (a, b) = (16.43, −2.12) as given in Table 4 of MB16. It is recommended that the FUV−J color lies strictly in the range of −0.97 to +6.66

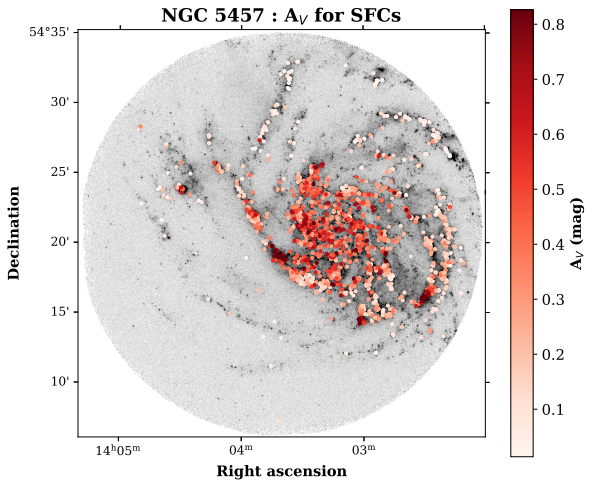


Figure 3. A_V map for the positions of NGC 5457's SFCs. Similar A_V maps for the remaining 16 galaxies are presented in Appendix E.

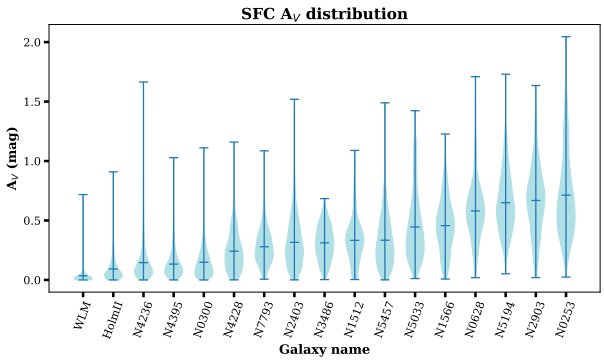


Figure 4. Violin plots for the A_V distribution of the observed SFCs in our 17 galaxies, arranged from left to right in increasing order of median A_V values. The central, top, and bottom bars represent the median, maximum, and minimum A_V values for the galaxy, respectively.

magnitude. Equations (1) and (2) can be used to estimate dust attenuation corrections in the FUV, NUV, and optical bands as follows:

$$A_{\rm FUV} = 2.5 * \log_{10}\left(1 + \frac{k_i * 24\mu \text{ luminosity}}{\text{FUV luminosity}}\right) \quad (3)$$

$$A_V = A_{\rm FUV}/R_{\rm FUV}, \quad A_{\rm NUV} = A_V * R_{\rm NUV}, \quad (4)$$

where $R_{\rm FUV}$ and $R_{\rm NUV}$ are attenuation coefficients for the FUV and NUV filters used, and are derived using Cardelli's law (J. A. Cardelli et al. 1989).

We used the above equations to create spatially resolved $A_{\rm FUV}$ or A_V maps of our sample galaxies. These maps are constituted by numerous square bins of 6″ angular resolution, spanning the entire extent of our galaxies. Only in the special case of WLM did we use a constant value of $k_{24\mu} = 3.89$, as WLM was not covered by the 2MASS survey in T. H. Jarrett et al. (2003). The 6″ angular resolution limit is set by the MIPS 24 μm data, which has the poorest resolution out of all the wave bands used in our $A_{\rm FUV}$ measurement. We matched the PSF of our FUV and J-band images to ∼6″ before the attenuation maps were generated. We present the A_V values at the SFC positions of NGC 5457 in Figure 3, and those for all the remaining galaxies in Appendix E. We also provide mathematical relations valid for different UVIT filters, which are used to convert source counts into various photometric units used (e.g AB magnitude, erg s^{-1}, and Jy) in Appendix F.

There are a few caveats associated with the attenuation correction calibration relations of M. Boquien et al. (2016), who cautioned that these relations should be used in the range of physical conditions in which they were derived. The relations were derived using early- and late-type spirals, so their use on irregular galaxies is slightly uncertain (our sample contains three irregular galaxies). They also cautioned the users about the presence of strong active galactic nuclei (AGN) which provide an additional dust heating mechanism, independent of stellar-driven heating. We note that the central few kpc bins in the k_i maps of AGN-hosting galaxies such as NGC 1566 and NGC 5033 were removed from our A_V maps because they fall outside of the $0.97 < \text{FUV} - J < 6.66$ magnitude color cut. This takes care of the AGN effect. Finally, their relations were derived at a few hundred parsec scale, and they advise against using the relations at much smaller scales, where the assumptions of fully sampled IMF and star formation history may break down. However, in the majority of our galaxies, the 6″ A_V bins correspond to a physical scale greater than 100 pc.

To assign an $A_{\rm FUV}$ value to a given SFC, we crossmatched the central SFC position with the 6″ bins in the A_V maps. Due to the 1.″5 angular resolution of the UVIT, as compared to that of the A_V map, our SFC sizes are typically smaller than the 6″ angular resolution A_V bin (6″ corresponds to ∼220 pc at the mean distance to the galaxies in our sample). In crowded regions, one 6″ A_V bin may have more than one SFC in it. In such cases, the same A_V value is assigned to each SFC. Therefore, our dust attenuation correction relies on the assumption that the A_V values do not vary significantly within our 6″ angular resolution limit. In Appendix G, we demonstrate how the potential variation in A_V within a resolution element does not significantly impact the SFC ages.

3.4.1. *Distribution of* A$_V$ *Values within Our Galaxies*

We created violin plots to describe the galaxy-wise A_V values presented in our catalog corresponding to the SFC positions within our galaxies (see Figure 4). This plot demonstrates the spread in the A_V values within our galaxies. The A_V distribution is arranged in increasing order of the mean A_V values. It shows that, on average, dwarf irregular galaxies have the smallest values of A_V, followed by the intermediate-mass flocculent spirals, and finally, the massive, classic spirals have the largest A_V values. The two galaxies with high inclination angles, i.e., NGC 2903 and NGC 0253 have the highest A_V values.

In Figure 5, we also present radial trends of the A_V values, distinguished by the three galaxy morphology types (as described in Section 2.1). These radial trends are generated by taking 15 bins, ranging from zero to the largest galactocentric radial distance at which an SFC is found, with each bin having an equal number of SFCs. The x-axis of these plots is normalized by the largest galactocentric radial bin. Before the radial trends are measured, the SFC positions are deprojected using the position angle and inclination angle values of the galaxies as given in Table 1, following the method outlined in Section 4.5 of Paper I.

We observed negative A_V gradients in nearly all of our spiral galaxies and the dwarf irregular galaxy NGC 4228. Similar negative A_V gradients for disk galaxies have also been observed in many studies, spanning a wide range of A_V measurement

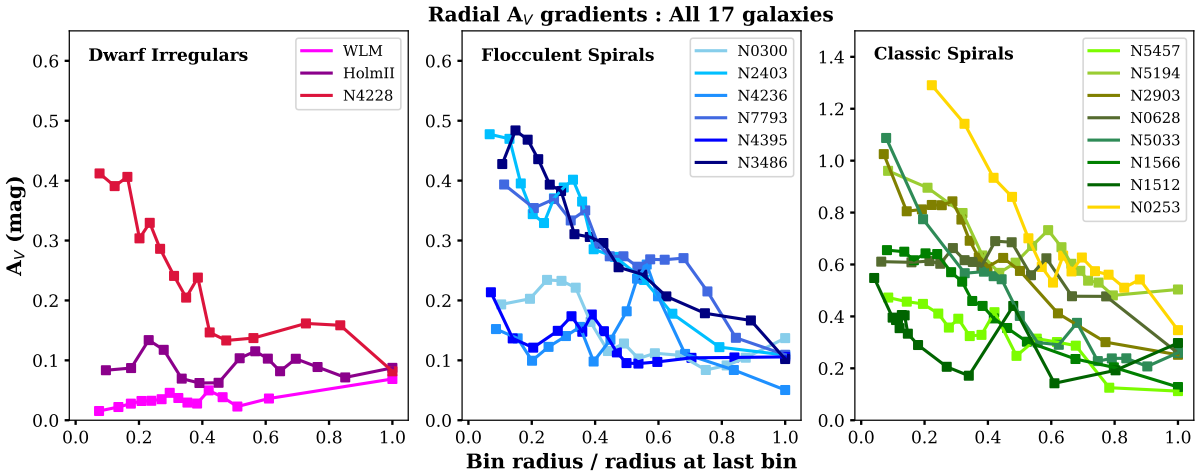


Figure 5. Radial A_V gradients with respect to the normalized galactocentric radius for our sample galaxies, separated by morphology.

techniques (K. Kreckel et al. 2013; M. Boquien et al. 2016; D. Kim et al. 2019; B. Groves et al. 2023). The two dwarf irregular galaxies WLM and Holmberg II deviate notably from this trend of negative A_V gradient, possibly owing to their unique irregular structure. The radial trends for A_V illustrate the distribution of the attenuating dust content within galaxies of different morphological types. We have already observed in Figure 4 that the mean A_V values of different galaxy types exhibit significant variations.

3.4.2. *Effect of Spatial Resolution on the Dust Attenuation Correction*

One of the highest spatial resolution attenuation maps (to the order of the UVIT spatial resolution) available in the literature is the one provided by the PHANGS Multi-Unit Spectroscopic Explorer (MUSE) survey (E. Emsellem et al. 2022; B. Groves et al. 2023). They provide A_V values for a large number of ionized nebulae, including H II regions, in 19 PHANGS-MUSE galaxies, measured using the Balmer decrement method. Three galaxies in our sample (NGC 0628, NGC 1512, and NGC 1566) are also part of the PHANGS-MUSE sample, and their catalog of H II regions was provided by F. Santoro et al. (2022). In order to check the effect of the spatial resolution of our attenuation maps on the SFC attenuation correction, we can compare our attenuation maps with those provided by the MUSE observations. However, due to the limited galaxy coverage of MUSE observations, the entire extent of these galaxies is not covered. Therefore, we can only compare the A_V values for the overlapping region between the UVIT and MUSE observations. We note that the attenuation maps compared here are derived using two different methods (one using UV and IR emission from the SFCs and the other using the Balmer decrement of H II regions), where the tracers and their lifetimes are different.

MUSE observations are taken from the 8.1 m Very Large Telescope and are assisted with adaptive optics. Therefore, they achieve an average angular resolution of $\sim 0\farcs7$, which is 1.5–2 times better than the UVIT's angular resolution. Additionally, these observations (suited to detect compact H II regions of luminosities in excess of a few times 10^{36} erg s^{-1}) are much more sensitive than our UV observations. For reference, this allows PHANGS-MUSE to characterize $\sim$2000 H II regions as compared to our $\sim$500 UV SFCs in the galaxy area common between PHANGS-MUSE and UV observations of NGC 0628. Due to the smaller number of SFCs characterized in NGC 1512 and the fact that only the inner star-forming ring of the galaxy is covered by PHANGS-MUSE observation, we restrict our A_V comparison analysis to only NGC 0628 and NGC 1566.

We crossmatched the UV SFC positions in R.A.–decl. coordinates with the H II regions identified in the two galaxies, to an accuracy of $\sim 1\farcs5$, which is closer to our UV angular resolution. This gives us two A_V values corresponding to roughly the same SFC position, measured using two different methods. In Figures 6 and 7, we demonstrate the results from our A_V comparison. The top rows (left) and (right) show the spatial A_V map derived using the Balmer decrement method for the H II regions and the measurement made in this paper for the SFCs following the MB16 method. We used the same color bar scaling in both images for an easier comparison, and we also quoted the mean A_V values in the figure title. It can be observed that the MB16-based A_V maps appear as slightly smoothed versions of the PHANGS-MUSE–based A_V maps. This is not surprising, considering that PHANGS-MUSE maps are created at better than $1''$ resolution, whereas the MB16-based maps are created at a poorer angular resolution of $6''$. Overall, we observe quite a good agreement in the spatial A_V maps as well as the mean values for both galaxies. This agreement is much better in NGC 0628. The bottom row (left) shows the histogram of the A_V values and the respective mean values of the distribution as vertical dashed lines. The bottom row (right) shows the trend of the A_V values with respect to the galactocentric radius. The spread of the A_V distribution as well as the overall shape of the radial A_V trend agree quite well between the two methods. Again, the agreement is much better in NGC 0628. Similar to the spatial maps, the bottom row plots also point toward good agreement between the A_V values measured by the two methods.

The observed small differences in the A_V comparison between the two methods could be due to the difference in the tracers (and their lifetimes) used to measure attenuation and the spatial resolution of the two A_V maps. Previous studies have also found that nebular-based attenuation gives higher values than the stellar-based measurements (J. Qin et al. 2019). The nebular-based attenuation values may be higher than the stellar-based values because Balmer decrement probes attenuation in dense, dusty, young star-forming regions, whereas the stellar-based attenuation combines the

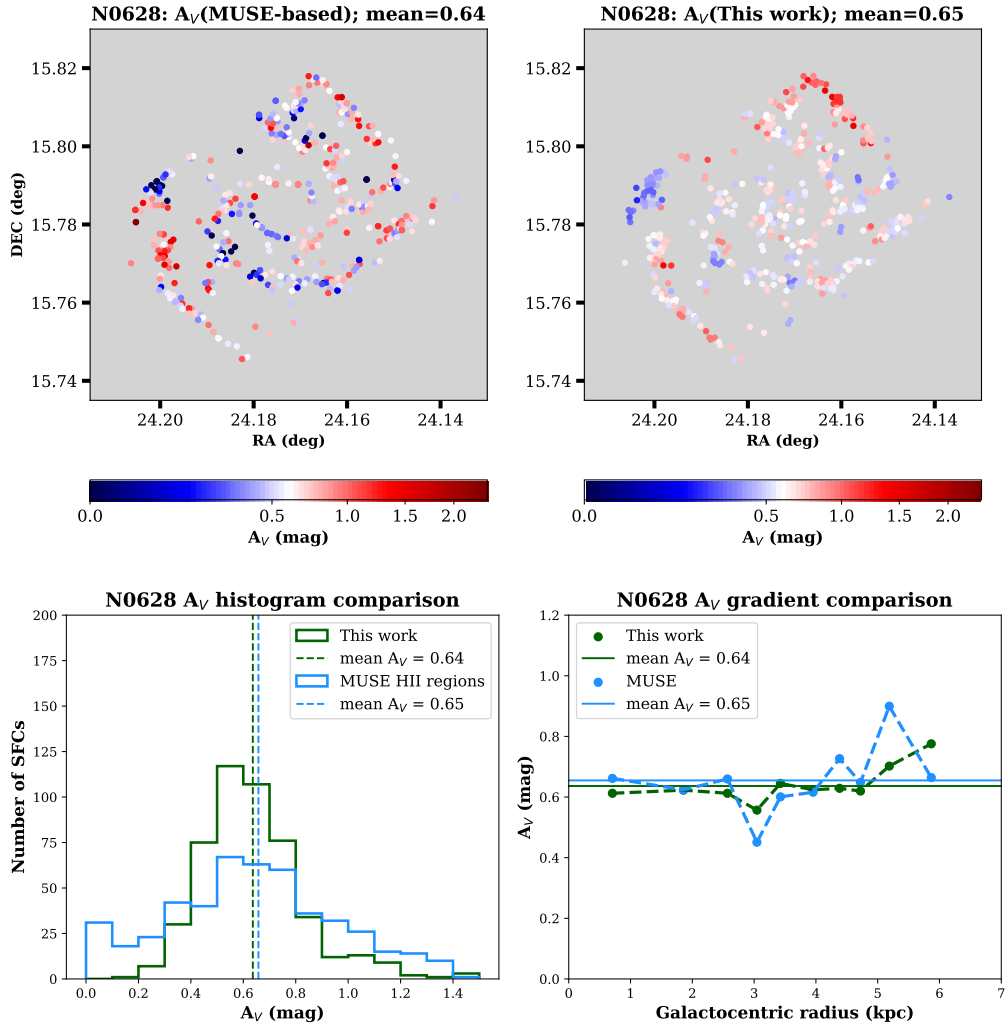


Figure 6. Illustrative figures showing the comparison of A_V measurements in NGC 0628 using MUSE-based H II regions (derived using the Balmer decrement method) and the method outlined by MB16 and used in this paper. This analysis is performed only in those parts of NGC 0628 that were covered in MUSE observations. Top row: spatial maps of A_V values measured at the location of the SFCs according to MUSE (left) and the MB16 method (right, this work). Bottom left: histogram of A_V values measured with MUSE (in green) and the MB16 method (sky blue). The mean and the range of A_V values match quite well between the two methods. Bottom right: radial profile of A_V values measured with the two methods. We observe mutually consistent trends between the two methods.

contributions from the dense, short-lived birth clouds and the diffuse dust permeating the ISM, which are heated by young and intermediate-age stellar populations (Y. Koyama et al. 2019). Overall, these observed differences are small and unlikely to significantly affect the age demographics presented in this paper.

Given the limited availability of high-resolution, full galaxy coverage NIR, MIR data, or dust attenuation maps, our current method of dust attenuation correction is the most that can be achieved within our current methodology, and it is clearly preferable over a constant or no dust attenuation correction. However, in the future, higher-resolution A_V maps of nearby galaxies could be created (at $\sim$1.″5 angular resolution) using UVIT FUV, full-galaxy-coverage James Webb Space Telescope (JWST) Near-InfraRed CAMera (NIRCAM) F115W and JWST Mid-InfraRed Imager (MIRI) F2100W filter observations.

3.5. Caveats on SFC Ages

We note that the FUV and NUV observations used in this study for our 17 galaxies are not from the same UVIT filters. From the multifilter, multiepoch UVIT observations taken for any galaxy, our filter choice aims to maximize the number of detected SFCs. However, due to the existence of the 2175 Å bump in Cardelli's Milky Way attenuation curve (which we have adopted in this study), the $R_{\rm NUV}$ value for some of our galaxies in the N219M, N242W, and N245M filters is comparable to the $R_{\rm FUV}$ value (see Table 2). In such galaxies, the reddening correction for the FUV−NUV color is much smaller than the other galaxies where N263M filter is used. According to our tests based on the galaxies with multifilter NUV observations, this implies that the derived SFC ages for such galaxies may be slightly overestimated and therefore should be treated as upper limits. Moreover, the synthetic SB99 UV CMD tracks for our galaxies are dependent on our choice of metallicity (see Table 3). J. Yadav et al. (2021) and C. Mondal et al. (2018) demonstrated that the synthetic FUV −NUV colors for an SFC of given age can vary if a different metallicity value is chosen in SB99. Although our adopted metallicity values for each galaxy are based on the latest reported values from the literature, we caution readers that, if a different value of metallicity is found to be more suitable for any of our galaxies, it would result in a change in the derived

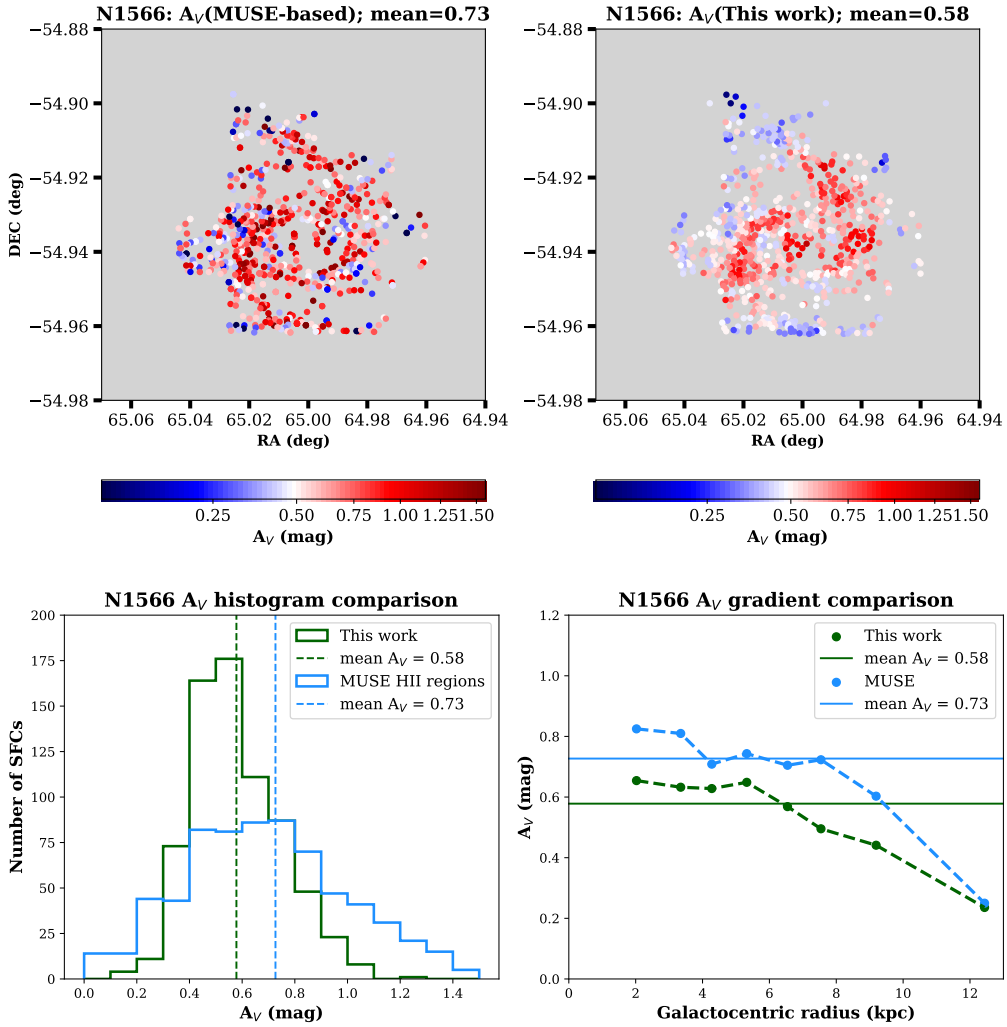


Figure 7. Same as Figure 6, but for NGC 1566. All four plots (spatial maps, mean value, range of values, and radial profile) indicate a reasonable match between the A_V values derived using the MUSE-based and MB16-based methods.

SFC ages. For an observed value of FUV−NUV color, an SB99 CMD constructed with a higher metallicity value than the value assumed in this paper would result in younger SFC ages and vice versa (J. Yadav et al. 2021).

3.6. Completeness Limit of SFCs

The completeness limits for the SFCs identified in each galaxy depend on several factors, such as the distance of the galaxy, the exposure time of the FUV and NUV observations, and the magnitude error cuts used to characterize the SFCs. In the nearest galaxies, luminous SFCs of small physical size will be easily detectable. However, similar SFCs located in farther away galaxies will be smaller than the resolution element, thereby avoiding detection. Additionally, these SFCs may be significantly fainter at these distances, and therefore will not survive the magnitude error cut. Only SFCs with sufficiently high signal-to-noise ratios survive the magnitude error cuts applied to each galaxy. Therefore, deeper exposure FUV and NUV images can reveal fainter SFCs, pushing the completeness limit to fainter magnitudes. This implies that the completeness limit for the SFCs identified in each galaxy will be different.

We used the method outlined in Section 4.4 of Paper I to measure the SFC completeness. We conducted tests in Paper I, by using UVIT images of NGC 7793 with different exposure times and plotting the attenuation-corrected FUV magnitude histogram of the identified SFCs. We found that the peak of the histogram systematically corresponds to fainter magnitudes, if deeper exposure images are used to characterize the SFCs. Therefore, the magnitude corresponding to the histogram peak may be considered as the completeness limit (D. A. Leahy et al. 2020; A. Devaraj et al. 2023; S. Hota et al. 2024b). This allowed us to measure the completeness limit FUV magnitude for each galaxy. Next, we measured the completeness limit age by measuring the age of a synthetic SB99 SFC of $10^4\,M_\odot$ and FUV magnitude equal to the attenuation-corrected completeness limit. We applied this method to all 17 of our galaxies, and in Table 2, we present the attenuation-corrected FUV magnitude value and the age (for an SFC of $10^4\,M_\odot$) corresponding to the completeness limit. Our SFCs are the most complete in galaxies such as WLM, Holmberg II, and NGC 0300 (a few hundred Myr), whereas they are the least complete in galaxies such as NGC 2903, NGC 0628, NGC 1512, and NGC 5194 (6–10 Myr). Overall, the combination of galaxy distance, exposure time,

and magnitude error cut are the primary drivers of the wide variation we observe in the completeness limits of the galaxies.

4. Age Demographics of SFCs within Galaxies

In this section, we present and interpret the observed age distribution of SFCs within our galaxies, with a special focus on the recent galaxy growth and assembly history across different morphologies. We reiterate that we have used UV observations for SFC identification, and our SFC ages are restricted to less than 400 Myr. Therefore, all of our age trends describe the recent star formation activity in galaxies, rather than their entire star formation history spanning several Gyr. Moreover, there exist partial/full galaxy coverage catalogs and age maps of stellar populations in the literature, for some of our galaxies. These catalogs differ from ours in terms of their spatial resolution, age range, age-estimation methodology, and the fraction of galaxy area being covered. Therefore, a direct comparison of our SFC ages with the ages presented in such catalogs would not be possible. However, wherever we discuss the age trends in this section, we present a qualitative comparison between our age demographic and those revealed using similar catalogs in the literature.

In Figure 8, we present the radial trends of the SFC ages within our galaxies, separated by the three galaxy morphology types (as described in Section 2.1). We followed the same method as the one used to measure the radial A_V trends in the Figure 5. A visual inspection of these gradients suggests negative age gradients in all of our sample galaxies. The observed slope of the age gradient is specific to the galaxy, and subtle variations in the shape of this gradient are attributed to the variation in the spiral structure of the galaxy at different galactocentric radii (L. Bianchi et al. 2005; D. A. Thilker et al. 2005b; J. C. Muñoz-Mateos et al. 2007; K. L. Barnes et al. 2011; T. Parikh et al. 2021).

We fitted the radial age gradient in each galaxy with a linear function. To perform the fitting, the change in SFC ages as a function of normalized galactocentric radius is measured. Since the UV extent of our galaxies can differ from R_{25}, the galactocentric radius was normalized with respect to the last radial bin ($R_{\rm last}$) used in measuring the age gradient. In Table 4, we show that the R_{25} and $R_{\rm last}$ of our galaxies are quite similar, barring NGC 1512, which has a highly disturbed and extended morphology. As our study is based on UV emission, the use of $R_{\rm last}$ over R_{25} is justified. Therefore the age gradient slope is measured in units of Myr/$R_{\rm last}$. Figure 8 shows the best-fit lines, and the corresponding slopes are provided in the legend. The best-fit slopes, R_{25}, and $R_{\rm last}$ are also tabulated in Table 4.

The inside-out growth scenario of galaxies is supported by the fact that all measured gradients are negative. We note that, because our galaxies span a wide range in size, the gradients presented are not absolute (i.e., in Myr kpc^{-1}). Instead, the Myr/$R_{\rm last}$ unit allows us to effectively compare the gradients across different galaxy morphologies, irrespective of galaxy size (interested readers can convert the Myr/$R_{\rm last}$ unit to Myr kpc^{-1} by multiplying the gradient slopes by $R_{\rm last}$). To compare the age gradient across morphological subclasses, we have plotted the individual gradient slopes in Figure 9. The three different morphological subclasses have been arranged separately in this figure, and individual galaxies are placed in ascending order of gradient slope. On average, the dwarf irregulars and intermediate-mass flocculent spirals exhibit shallower slopes (except the dwarf irregular NGC 4228, which exhibits a significantly steep negative gradient) as compared to the massive, classic spirals. This figure provides evidence for both galaxy-to-galaxy and morphology-dependent variations in age gradients. The powerful combination of UVIT's 28′ FoV and 1.″5 angular resolution has enabled us to systematically characterize the SFCs and investigate the age gradients. Performing such an analysis on our sample of 17 galaxies would have been challenging with the HST, due to its FoV limitation, or with GALEX, due to its poorer, $\sim$5″ angular resolution.

In the upcoming sections, we discuss the spatial age maps of galaxies, their connection with galaxy morphology, and the probable physical reasons for the observed age demographic.

4.1. Spiral Galaxies

The spatial age maps (Figures 10 and 11) for the majority of our spiral galaxies point toward the existence of a negative radial age gradient where the majority of the old SFCs (red colored points) are located at smaller galactocentric radii and young SFCs (blue colored points) are predominantly found at larger radii. (From this section onward, the classification of SFCs as "young" or "old" SFCs is made in a relative sense. We note that all these SFCs together represent stellar populations that have formed recently, i.e., within the past 400 Myr).

Clear negative age gradients were observed in all of our spiral galaxies (see the best-fit lines and slope values in Figure 8), which is a well-established signature of inside-out growth mechanism of disk galaxies—the galaxies acquire their inner regions quite early in their evolutionary history, and their outer regions (that still harbor active star formation) are accumulated by continuous accretion of gas from the intergalactic medium in the later stages of the galaxy's evolution (R. B. Larson 1976; S. D. M. White & C. S. Frenk 1991; H. J. Mo et al. 1998; T. Naab & J. P. Ostriker 2006). In the inside-out growth scenario, either the star-forming gas does not accumulate in the outer parts of galaxies until later times, or the star formation timescales in outer disks are longer. This scenario leads to predictions of negative age and metallicity gradients in galaxies, which have now been proven observationally using FUV and NUV data from GALEX (L. Bianchi et al. 2005; D. A. Thilker et al. 2025a, 2005b; J. C. Muñoz-Mateos et al. 2007; K. L. Barnes et al. 2011), using HST observations (S. M. Gogarten et al. 2010; D. J. Radburn-Smith et al. 2012; E. Sacchi et al. 2019), and using integral field unit observations (R. García-Benito et al. 2017).

We observed that the youngest SFCs are often cospatial with the position of spiral arms at all radii, in all spiral galaxies. This highlights the crucial role that spiral arm driven physical processes, such as spiral wave compression, shocks, and cloud collisions, play in the formation of the youngest stellar populations in a galaxy (C. C. Lin & F. H. Shu 1964; A. B. Romeo & N. Falstad 2013; D. M. Elmegreen & B. G. Elmegreen 2014; A. B. Romeo & K. Fathi 2016; A. B. Romeo & K. M. Mogotsi 2017; F. Shabani et al. 2018; C. Mondal et al. 2021; J. Yadav et al. 2021; K. Ujjwal et al. 2022). It can also be observed that the slightly older SFCs are located away from the spiral arms. This is consistent with the picture that it takes stars a few tens of Myr to traverse the

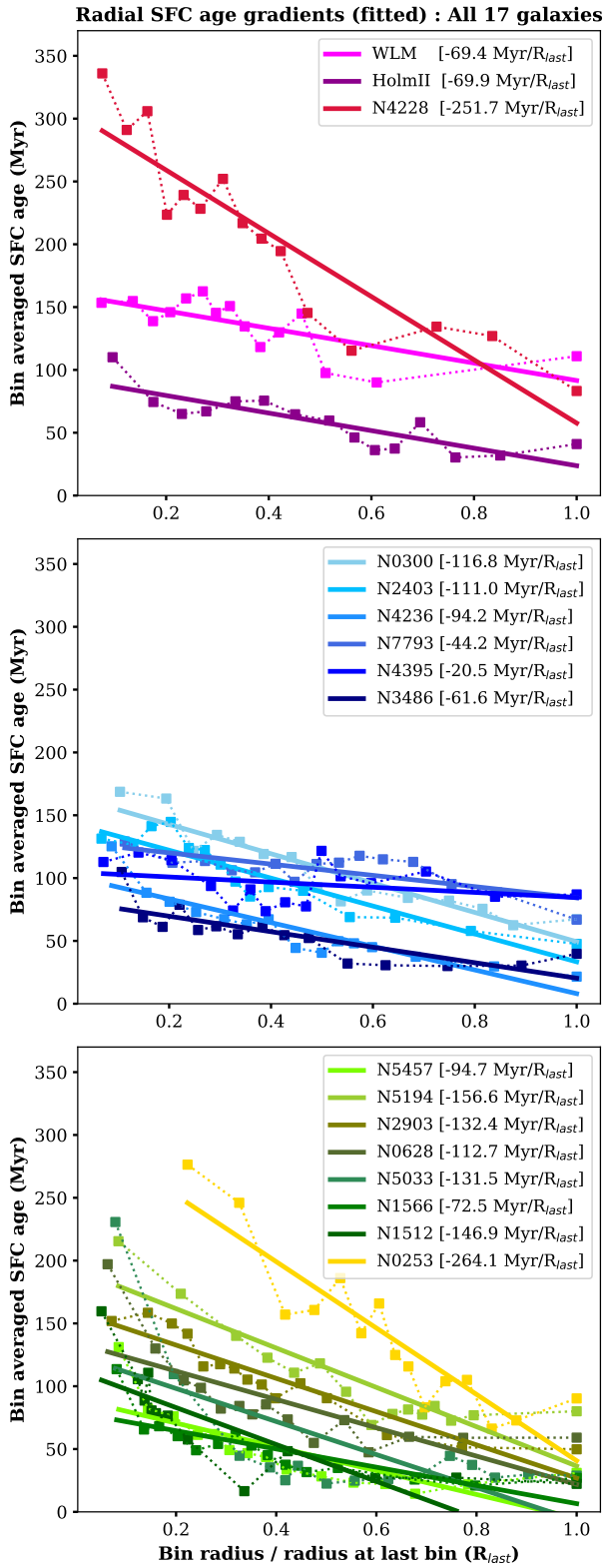


Figure 8. Radial SFC age gradients with respect to the normalized galactocentric radius for our sample galaxies, separated by morphology. The gradients are fitted with a linear function, and the best-fit slopes are given in the legend.

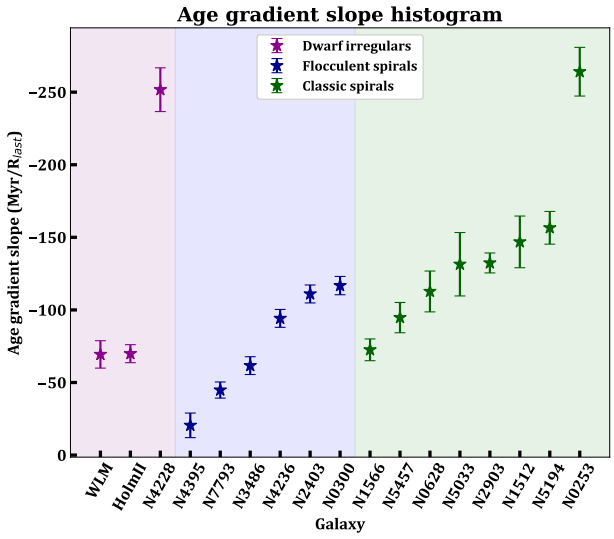


Figure 9. Histogram of the radial SFC age gradient slopes for our galaxies. Colored vertical bands are added to distinguish among morphological subclasses. Galaxies belonging to a particular morphological subclass are arranged in ascending order of gradient slope.

Table 4
Galaxy Properties and Corresponding Radial Age Gradient Slopes

Galaxy	$R_{\rm last}$ (kpc)	R_{25} (kpc)	Slope (Myr/$R_{\rm last}$)
WLM	2.08	1.8	−69.4
Holmberg II	4.02	3.7	−69.9
NGC 4228	4.25	2.9	−251.7
NGC 0300	6.72	5.9	−116.8
NGC 2403	10.44	7.3	−111.0
NGC 4236	12.8	15.2	−94.2
NGC 7793	5.34	4.9	−44.2
NGC 4395	7.85	8.2	−20.5
NGC 3486	11.02	11.7	−61.6
NGC 5457	22.74	27.9	−94.7
NGC 5194	9.21	13.9	−156.6
NGC 2903	16.02	17.4	−132.4
NGC 0628	13.14	15.0	−112.7
NGC 5033	27.17	29.7	−131.5
NGC 1566	22.64	21.4	−72.5
NGC 1512	49.2	23.1	−146.9
NGC 0253	11.78	14.4	−264.1

spiral arm of a galaxy. As the neutral hydrogen (H I) disks of galaxies are much more extended than their stellar disks, the presence of young SFCs at large galactocentric radii may also be indicative of the cold gas accretion and its subsequent collapse to form young stars (J. Kormendy 2013; S. H. Ho et al. 2019).

The flocculent spiral galaxy NGC 7793 shows a nearly uniform distribution of young and old SFCs as a function of radius, and it exhibits one of the shallowest age gradients in our sample. C. Mondal et al. (2021) have shown that the scale radius of NGC 7793 increases from optical to NUV to FUV wave bands, indicating inside-out growth. Similarly, E. Sacchi et al. (2019) found evidence for inside-out growth of NGC 7793 by analyzing resolved star formation history in different regions of the galaxy using the LEGUS-HST data. However, it appears that the negative age gradient (inside-out growth indicator) in this flocculent spiral galaxy is not as prominent as in the majority of the spiral galaxies in our sample. D. A. Thilker et al. (2005a, 2005b) have shown that, typically, the stellar population in galaxies is found to be younger with increasing galactocentric radius, but the steepness of this effect can vary from galaxy to

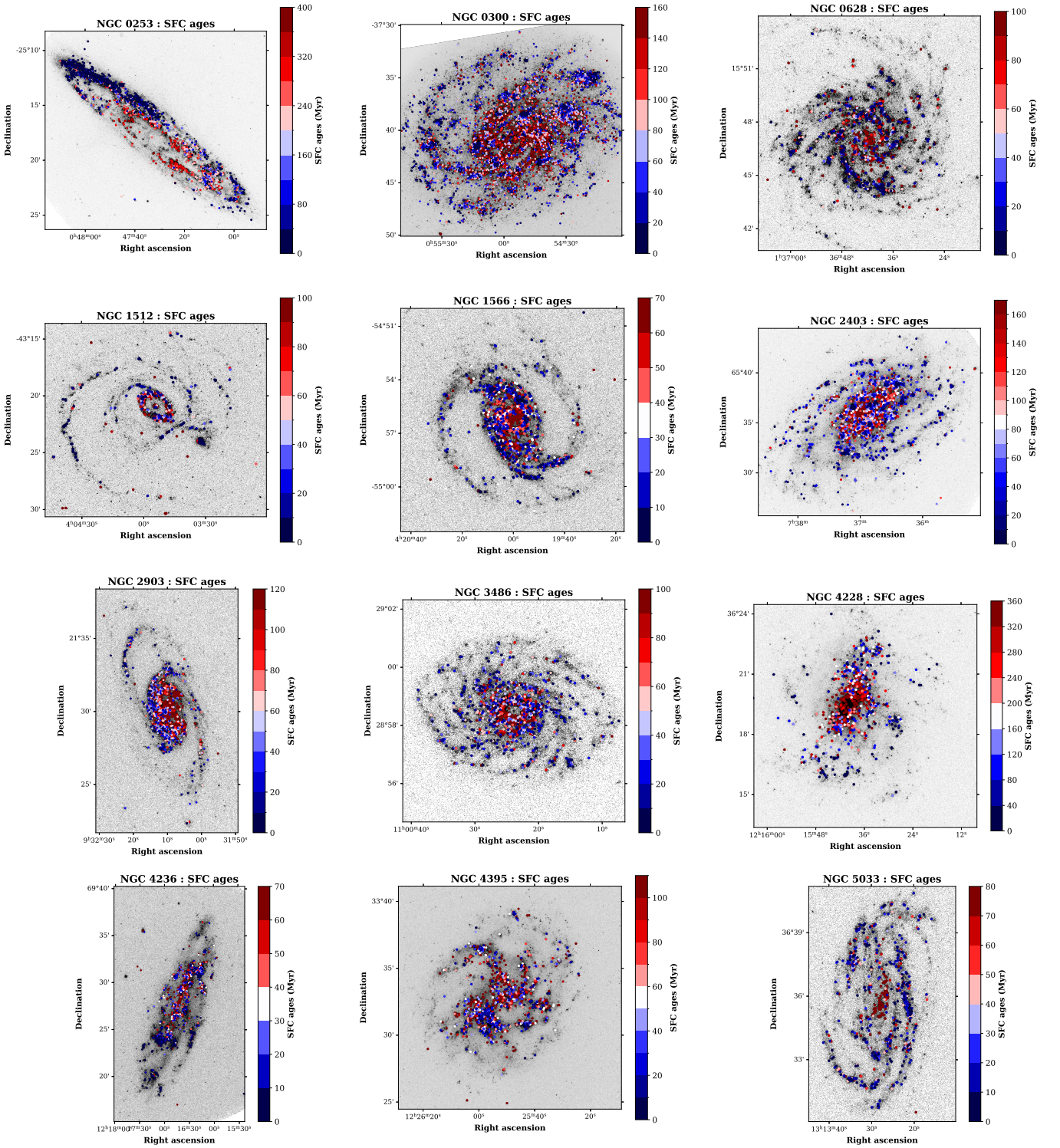


Figure 10. The derived age maps of the SFCs characterized in 12 out of the 17 galaxies. The color bar represents SFC ages. We chose arbitrary age ranges in the color bars in order to highlight the contrast between the positions of young and old SFCs, all formed within the past 400 Myr. The complete list of the photometric properties and ages of these SFCs is presented with this paper, and it can be accessed from the machine-readable table associated with Table 6.

galaxy. In another flocculent spiral galaxy, M33 (not studied in this paper), for instance, the negative age gradient was found to be small, and the FUV−NUV color remained roughly constant over a large range of galactocentric radius. This implies that the star formation activity in the galaxy over the past ∼200 Myr has been globally spread out. NGC 7793 may be experiencing the same phenomenon.

The young SFCs in NGC 7793 show good cospatiality with its flocculent spiral arms, which agrees with similar observations made by K. Grasha et al. (2018), C. Mondal et al. (2018), F. Shabani et al. (2018), and E. Sacchi et al. (2019). Flocculent arms of a galaxy are believed not to be created by any coherent spiral wave; rather, gas collapses along the clumpy, disjointed, flocculent arms of the galaxy under the action of local

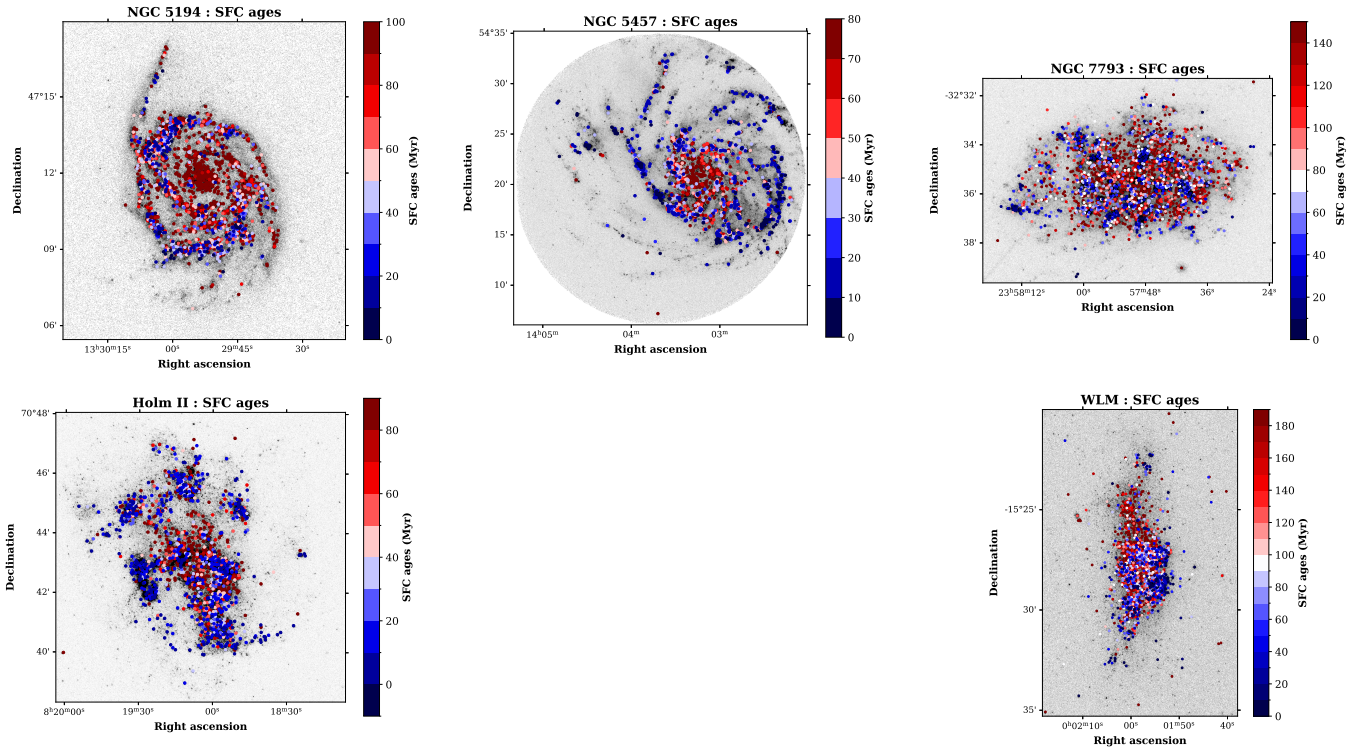


Figure 11. The derived age maps of the SFCs characterized in the remaining five out of the 17 galaxies.

gravitational instabilities (B. G. Elmegreen et al. 2006; A. B. Romeo & N. Falstad 2013; D. M. Elmegreen & B. G. Elmegreen 2014; K. Fathi et al. 2015; D. A. Goulier-mis 2018). This leads to star formation along the flocculent arms of such galaxies, and the young SFC distribution of the flocculent spirals in our sample—NGC 0300, NGC 2403, NGC 3486, and NGC 7793—clearly demonstrates this phenomenon.

For two of our most inclined galaxies, NGC 2903 and NGC 0253, we observed a rough division of young and old SFCs in our age maps, where SFCs on one side of the major axis are predominantly old (e.g., the southeastern half of NGC 0253 and the northwestern half of NGC 2903), and SFCs on the other side of major axis are predominantly young (e.g., the northwestern half of NGC 0253 and the southeastern half of NGC 2903). These observations are unlikely to be physical in nature. We believe that such trends can be driven by insufficient dust attenuation correction, due to the galaxy's high inclination. In such a scenario, diffuse dust located above or below the galaxy's thin stellar disk can cause the SFCs on the far side of the galaxy to suffer much more attenuation, so they consistently appear older (as the light path length traversing through the dust is longer), as compared to the SFCs on the near side, which consistently appear younger. K. Kreckel et al. (2013) observed a similar contrast between the near- and far-side dust attenuation values for the highly inclined galaxies NGC 2146 and NGC 7331, which supports our reasoning. The spatial age map of NGC 0253, in particular, appears to be the most affected by its high inclination induced attenuation problem. The young SFCs on the northeast side of the galaxy appear to be younger (darker shade of blue) than the young SFCs on the southwest side (lighter shades of blue). T. J. Davidge (2010) have suggested that the high dust content of NGC 0253 strongly affects its appearance in UV wavelengths. Our A_V maps (Figure 15, first figure) and median A_V values (Figures 4) prove that, among our galaxy sample, NGC 0253 suffers the most strongly from dust attenuation. We posit that perhaps the unaccounted-for dust attenuation between the near and far sides of our inclined systems NGC 2903 and NGC 0253 can give rise to the observed division between the SFC ages with respect to the galaxies' major/minor axes. This behavior of NGC 2903 and NGC 0253 points toward a limitation in our dust attenuation correction method in highly inclined galaxies. However, age determination for highly inclined galaxies can prove challenging even with the most sophisticated age-determination techniques (K. Kreckel et al. 2013; MB16).

4.2. *Dwarf Irregular Galaxies*

The three dwarf irregular galaxies in our sample show quite diverse age demographics (see spatial age maps in Figure 10 and 11). In NGC 4228, the old SFCs appear to be uniformly distributed in the main body of the galaxy, and most of the SFCs that are located in the patchy outskirts of the galaxy appear to be young. This is similar to the behavior shown by the spiral galaxies in our sample—consistent with the inside-out growth scenario. In Holmberg II, both the young and old SFCs can be observed at all galactocentric radii. However, its young SFCs appear to be clustered together into distinct groups, in particular in the patchy outskirts of the galaxy. Its old SFC population appears to be uniformly distributed within the galaxy, and their distribution follows what appears to be the main body of the galaxy. For comparison, in another galaxy, NGC 1313, which has an irregular, disturbed morphology in its outskirts quite similar to that of Holmberg II, S. Ananthu et al. (2026) recently studied the age demographics using UV and optical data. They too found that, similar to Holmberg II, the irregular, patchy outskirts of NGC 1313 host the youngest stellar populations, whereas the old SFCs dominate the stellar population in the inner regions of the galaxy. Finally,

in WLM, the old SFC population can be found all over its main body, and some isolated, old SFCs are scattered farther away from the galaxy, too. The young SFCs of WLM are clustered together in three to four regions in the southern half of the galaxy, and one clustering of young SFCs can be observed at the northern most part of the galaxy.

C. L. Riggs et al. (2024) (and references therein) suggest that dwarf galaxies, too, are formed inside out and are expected to exhibit negative age gradients. This is supported by our observed age-gradient slopes. However, in dwarf galaxies, bursty star formation can induce strong stellar feedback that imparts outward momentum to star-forming gas. The stars formed from this gas will migrate toward outer regions, owing to their inherently outward radial velocity. This can flatten or even erase the negative age gradient in dwarf galaxies, which may explain why the age-gradient slopes of Holmberg II and WLM are shallower than those of our massive spiral galaxies. However, this mechanism may not be strong enough to produce the same effect in large, spiral galaxies (A. S. Graus et al. 2019). Overall, the diversity in the distribution of different-aged stellar populations in our small sample of three dwarf irregular galaxies may be indicative of their more complex galaxy assembly history, as compared to the spiral galaxies in our sample. Our age maps for dwarf irregular galaxies also appear to be consistent with the stochastic nature of star formation in them—often triggered by internal processes such as local gas instabilities and stellar feedback (D. Williamson et al. 2016; C. Mondal et al. 2018; D. O. Cook et al. 2019; S. Amrutha et al. 2024).

5. Summary and Future Plans

In this paper, we have presented a complete galaxy coverage, FUV- and NUV-based catalog of ∼25,000 recently formed ($\lesssim$400 Myr) star-forming clumps (SFCs) in 17 nearby galaxies. The production of this catalog is motivated by a dearth of systematic UV-based studies of recent star formation at high spatial resolution in a large, diverse galaxy sample (spanning a wide range in morphology and mass) with a homogeneous methodology (including SFC detection, characterization, and a treatment of spatially varying dust attenuation correction). Such studies are needed in order to better understand the different galaxy environments and physical processes responsible for galaxy evolution, e.g., starbursts, feedback, interactions, and quenching.

Our sample of 17 galaxies, all located within 20 Mpc, includes eight massive, classic spiral galaxies, six intermediate-mass, flocculent spiral galaxies, and three dwarf irregular galaxies. In this work, we have utilized the 1.″5 angular resolution, archival FUV and NUV observations of our galaxies from UVIT (A. Kumar et al. 2012). We used the Astrodendro package on the UVIT FUV images of our galaxies to identify SFCs using a homogeneous detection criteria. We performed photometry on the FUV and NUV images to estimate the corresponding magnitudes of the SFCs. Next, by comparing dust attenuation corrected, observed UV CMDs against the synthetic Starburst99 simple stellar population model UV CMD (C. Leitherer et al. 1999), we estimated the ages of the identified SFCs. The dust attenuation correction was performed in a spatially resolved manner, all the while accounting for the age dependence of the attenuation correction calibration coefficients. For this purpose, we followed the method outlined by M. Boquien et al. (2016) and utilized a combination of UVIT FUV, 2MASS *J*-band, and MIPS 24 μm observations to create full galaxy coverage, 6″ angular resolution A_V maps for our 17 galaxies. We applied FUV and NUV magnitude error cuts on the detected SFCs, so as to choose only the brightest SFCs with reasonably small age errors in the finalized SFC catalog. This ultimately led to an extensive, finalized catalog of ∼25,000 SFCs. We make our SFC catalog and A_V maps (as value-added products) for the 17 galaxies publicly available with this paper.

Along with presenting the methodology for constructing the SFC catalog, we have also provided a discussion of the age demographics of different stellar populations in our galaxies. This discussion focused on the insights these age distributions can provide on galaxy growth, assembly history, the role of spiral arms in star formation, and the different drivers of star formation in galaxies of varied morphology and mass. With our age maps, we found trends consistent with several well-established phenomena spanning the entire galaxy mass and morphology range, such as the inside-out growth of disk galaxies, association of spiral arms with star formation, local gravitational instabilities causing star formation in the flocculent spiral arms, and the stochastic nature of star formation in dwarf galaxies. As our galaxy sample lies between 1 and 20 Mpc, the identified SFCs using UVIT's ∼1.″5 resolution data likely correspond to different physical structures across the sample (e.g., individual clusters, stellar associations, and extended unbound complexes). In Appendix H, we test the robustness of our results by degrading higher-resolution images to a common physical scale and demonstrate that our main trends are not driven by resolution effect.

In the future, this catalog can be coupled with the insights drawn from multiwavelength data to improve the understanding of many other aspects of galaxy evolution, such as the impact of galactic dynamics on different stellar populations within galaxies, secular versus interaction-driven galaxy evolution, enhancement/quenching of star formation, and the UV luminosity function of star-forming regions in galaxies. Though the SFC catalog generated in this study is at ∼1.″5 angular resolution, due to our full galaxy coverage and our use of FUV data, this catalog can serve as a complementary resource to the excellent star cluster catalogs being created by large galaxy surveys such as LEGUS (D. Calzetti et al. 2015), PHANGS (J. C. Lee et al. 2022), and the Galaxy UV Legacy Project (GULP) (PI: Elena Sabbi; E. Sabbi et al. 2026), to name a few.

In G. Shashank et al. (2025) (Paper I), we demonstrated with a pilot sample of four galaxies that UVIT's high resolution, FUV coverage, and large 28′ field of view uniquely allows us to characterize the star formation hierarchies in galaxies over scales ranging from tens of parsecs up to tens of kiloparsecs. The current paper (Paper II) aims to aid the expansion of the work done in Paper I onto this larger sample of 17 galaxies, with the advantage of a greater morphological diversity. In Paper III (G. Shashank et al. 2026, in preparation), we have utilized this SFC catalog to derive new insights about stellar hierarchies of these 17 galaxies, such as their limiting scale within galaxies, dispersal timescales, and how these are affected by host galaxy properties (stellar mass, size, shear, and nature of spiral arms). In the future, we will target a preselected sample of ∼30 more galaxies, which have archival UVIT FUV-only observations. We will combine UVIT FUV data with multiband optical, narrowband Hα, and multiband

IR observations, and characterize the SFC populations in these galaxies using the Code Investigating GALaxy Emission (CIGALE; M. Boquien et al. 2019) SED-fitting tool. Our overarching goal with this larger sample will be to improve our understanding of the stellar population demographic and star formation hierarchies in nearby galaxies—spanning an even broader parameter space in morphology, mass, size, and metallicity.

Significant improvements could be made in our methodology by using a higher-resolution ultraviolet imaging telescope with FUV and NUV imaging capabilities and a large field of view. With only a single pointing, such a telescope should allow the detection and characterization of thousands of parsec-scale, young star clusters within the full spatial extent of nearby galaxies. To this end, future missions such as the INdian Spectroscopic and Imaging Space Telescope (INSIST) (A. Subramaniam 2022) and Cosmological Advanced Survey Telescope for Optical and Ultraviolet Research (CASTOR) (P. Côté et al. 2025) will allow us to observe a larger, untapped reservoir of star-forming galaxies (which do not have existing high-resolution UV observations) in the local Universe and further our knowledge of star formation related phenomena in galaxies. INSIST's proposed subarcsecond angular resolution will also facilitate the study of different stellar populations in galaxies beyond 20 Mpc and up to a few hundred Mpc.

Acknowledgments

G.S. and S.S. thank Dr. Alessandro Boselli and Dr. Médéric Boquien for their constructive suggestions regarding the dust attenuation corrections, which were crucial in constraining the SFC ages. G.S. also thanks D. Renu, Rakshit Chauhan, and Sanal Ananthu for their help duing UVIT data analysis. G.S. and S.S. also acknowledge the PIs of the UVIT data used in this paper for targeting these majestic galaxies and making this work possible. S.S. acknowledges support from the Science and Engineering Research Board of India through the POWER research grant (SPG/2021/002672) and support from the Alexander von Humboldt Foundation. S.H.M. acknowledges the support of NASA grant No. 80NSSC20K0500, NSF grant AST-2009679, and the Simons Foundation. C.M. acknowledges support from the National Science and Technology Council, Taiwan (grant NSTC 112-2112-M-001-027-MY3) and the Academia Sinica Investigator award (grant AS-IA-112-M04).

Software: Python (G. Van Rossum & F. L. Drake 2009), ASTROML (J. VanderPlas et al. 2012), scikit-learn (F. Pedregosa et al. 2011), Matplotlib (J. D. Hunter 2007), NumPy (C. R. Harris et al. 2020), SciPy (P. Virtanen et al. 2020), AstroPy (Astropy Collaboration et al. 2018), Astrodendro (http://www.dendrograms.org/), photutils (L. Bradley et al. 2024), and CCDLAB (J. E. Postma & D. Leahy 2017).

Data Availability

This publication uses data from the UVIT—one of the five science instruments on board the AstroSat satellite of the Indian Space Research Organization (ISRO). The UVIT data are archived at the Indian Space Science Data Centre (ISSDC). The level 1 UVIT data for our galaxies can be extracted at (https://astrobrowse.issdc.gov.in/astro_archive/archive/Home.jsp) using the galaxy name and R.A., decl. information given in Table 1. The science-ready NIR and MIR images used in this paper were directly taken from the NASA Extragalactic Database (NED).

Appendix A
Astrodendro Sensitivity Analysis

To address the robustness of SFC detections as a function of variation in astrodendro parameters, we performed the following sensitivity analysis. NGC 7793 was selected for this, due to its proximity and higher exposure data. We separately varied the detection threshold (min_value), contrast (min_delta), and number of pixels (min_npix) by a few times and tabulated the number of leaves and SFCs with photometric uncertainties smaller than 0.10 mag (see Table 5). Additionally, we also varied all three parameters simultaneously by a factor of 2. We observed a small loss (0%–25%) in the surviving number of SFCs as higher values of astrodendro parameters are used. We conclude that the surviving number of SFCs is not very sensitive to the variation in the astrodendro parameters, at least by a factor of 2.

Next, we visually inspected the spatial age map created at the (1bg + 3σ, 1σ, 11 px) astrodendro parameters with the map created at (2 bg + 6σ, 2σ, 22 px) parameters. A strong

Table 5
Astrodendro Parameters and the Corresponding Number of Leaves and SFCs in Our Sensitivity Analysis

Category	min_value	min_delta	min_npix	Number of Leaves	Number of SFCs
Used in the paper	1bg + 3σ	1σ	11	8177	1775
min_value variation	1bg + 5σ	1σ	11	6186	1759
	1bg + 10σ	1σ	11	3765	1664
	1bg + 20σ	1σ	11	2061	1404
min_delta variation	1bg + 3σ	3σ	11	7964	1780
	1bg + 3σ	5σ	11	6621	1798
	1bg + 3σ	10σ	11	3184	1924
min_npix variation	1bg + 3σ	1σ	22	3939	1661
	1bg + 3σ	1σ	33	2599	1444
	1bg + 3σ	1σ	44	1920	1262
All parameters varied	2bg + 6σ	2σ	22	2577	1587

Note. Counterintuitively, when the min_delta value is increased, the number of surviving SFCs increases. This is because the detected leaf sizes increase and thus more SFCs can survive the 0.10 magnitude error cut.

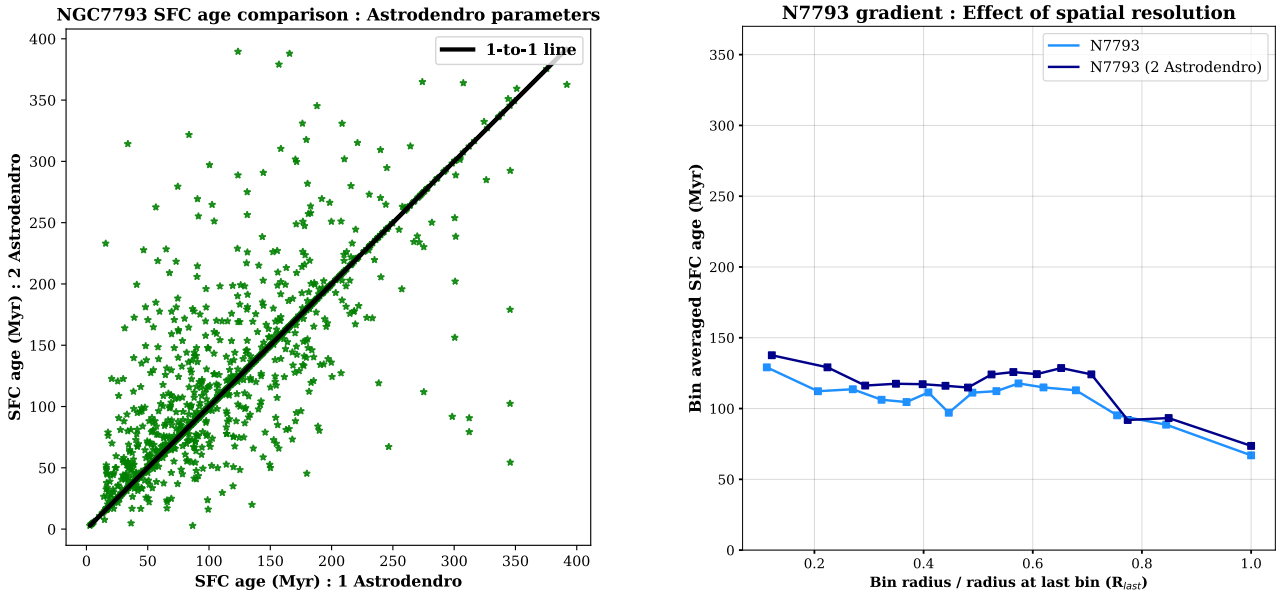


Figure 12. Left: comparison of SFC ages in NGC 7793, measured at (1bg + 3σ, 1σ, 11 px) (x-axis) and (2 bg + 6σ, 2σ, 22 px) astrodendro parameters. A good one-to-one correlation is observed. Right: radial SFC age gradient for NGC 7793 created using the (1bg + 3σ, 1σ, 11 px) (light blue) and (2 bg + 6σ, 2σ, 22 px) (dark blue) astrodendro parameter choices. The shape of the radial age gradient is preserved, with slightly older ages measured for higher astrodendro parameters.

match in the location of young and old SFCs was observed. A strong one-to-one correlation in the SFC ages was also observed (see Figure 12 (left)). Additionally, the shape of the radial age gradient was preserved, with slightly older ages measured for higher astrodendro parameters (see Figure 12 (right)). This demonstrates that the main conclusions of our paper are robust to reasonable variations in the astrodendro parameters. Similar conclusions were drawn in C. Mondal et al. (2021) regarding the effect of varying astrodendro parameters on the resulting number of SFCs and their properties.

Appendix B
Effect of Adopting More than One Metallicity Value in SB99 to Account for Radial Metallicity Gradients

As the existence of negative metallicity gradients is well established in disk galaxies, the metallicity adopted to simulate the SFCs in SB99 should ideally vary with galactocentric radius. However, the metallicity choices available in SB99 are quite sparse, with only $Z = 0.001$, 0.004, 0.008, 0.02, and 0.04 as options. Consider NGC 0628 and NGC 1566, both of which have stellar masses greater than $10^{10}\,M_{\odot}$, and therefore we adopted a metallicity value of $Z = 0.02$ for these galaxies. F. Santoro et al. (2022) measured the metallicity gradients to be $12 + (\mathrm{O/H}) = 8.53 - 0.014\,R_{\rm gal}$ for NGC 0628 and $12 + (\mathrm{O/H}) = 8.62 - 0.012\,R_{\rm gal}$ for NGC 1566, in their Figure A.19. Here, $R_{\rm gal}$ is the galactocentric radius. Now consider NGC 7793, for which L. Della Bruna et al. (2021) measured median $12 + (\mathrm{O/H}) = 8.37$. The stellar mass of NGC 7793 is $\times\,10^{9}\,M_{\odot}$ and we adopted $Z = 0.008$ for this galaxy (similar to C. Mondal et al. 2021). The sparse metallicity grid available in SB99 meant that, for NGC 7793, we could only choose $Z = 0.008$. Using the metallicity gradient relations above, the $12 + (\mathrm{O/H})$ value of NGC 0628 and NGC 1566 will fall to 8.37 (equivalent to $Z = 0.008$, i.e., NGC 7793's metallicity) at $R_{\rm gal} = 11.4$ kpc and 21.4 kpc. These radii are comparable to the R_{25} of the galaxies, i.e., 15 kpc for NGC 0628 and 21 kpc for NGC 1566. This demonstrates that the observed metallicity gradients are not steep enough to justify the use of two different SB99 metallicity values in the inner and outer regions of a galaxy. Therefore, our choice of adopting a single metallicity value for each galaxy is reasonable. Even in past literature, when star clusters are characterized using spectral energy distribution fitting, only one metallicity value per galaxy is used (A. Adamo et al. 2017; S. H. Menon et al. 2021; J. A. Turner et al. 2021; S. T. Linden et al. 2022). In such works, the main focus is on breaking the age–extinction degeneracy and not on constraining the metallicity effectively.

However, to constrain the maximum variation possible in SFC ages with two different metallicity values being used in a galaxy, we performed the following test. It is well established that using lower metallicity for a simulated star cluster (in SB99) leads to bluer colors. In our tests, the UV CMD demonstrated this effect, when simulated evolutionary tracks for solar metallicity ($Z = 0.02$, solid lines) and subsolar metallicity ($Z = 0.008$, dashed lines) were plotted together. As a result, for a given FUV–NUV color, the derived SFC age should be older at a lower, subsolar metallicity. Next, we assumed $Z = 0.02$ in the inner parts (galactocentric radius $< R_{25}/2$) of NGC 5457 and $Z = 0.008$ in the outer parts. We created spatial age-difference maps and histograms with respect to the SFC ages measured assuming a single metallicity value of $Z = 0.02$ across the entire galaxy (the ages used in the paper). This way, only the outer SFCs are expected to exhibit age differences. The age-difference map and histogram suggest that lower metallicity leads to older SFC ages within an age range of ∼0–25 Myr (see Figure 13).

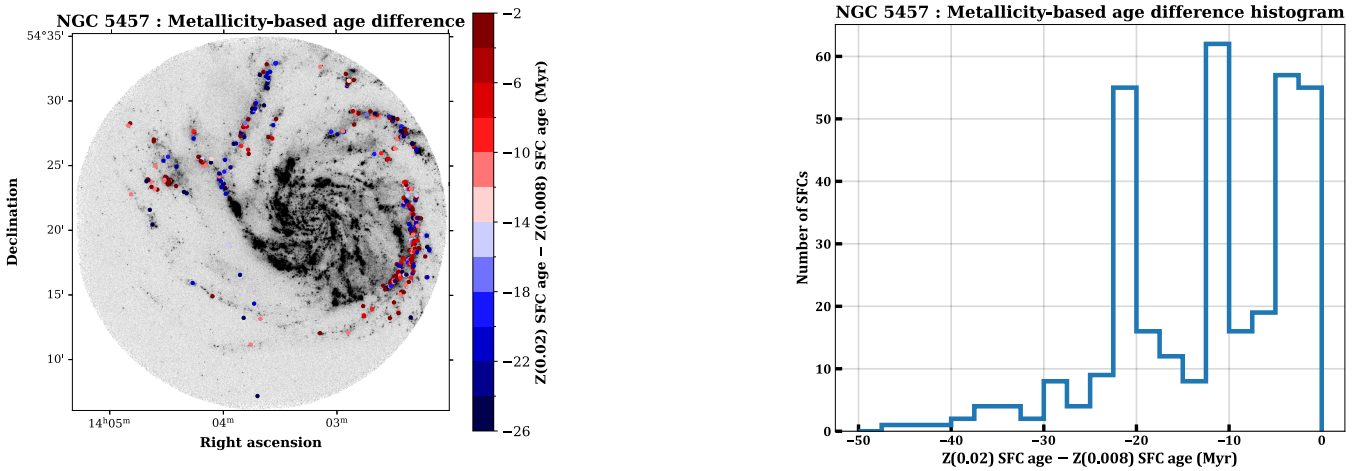


Figure 13. Spatial age-difference map (left) and age-difference histogram (right) for SFCs in NGC 5457, assuming $Z = 0.02$ in the inner parts (galactocentric radius $<R_{25}/2$) and $Z = 0.008$ in the outer parts (galactocentric radius $> R_{25}/2$) of the galaxy. Age differences in the range of 0–25 Myr are observed.

Appendix C
SFC Catalog Table

In Table 6, we present a brief description of the properties of the first SFC for each of our 17 galaxies. The full SFC catalog consists of ∼25,000 SFC within our 17 galaxies.

Table 6
Description of the Physical Properties of the ∼25,000 SFC Characterized within Our 17 Galaxies

Galaxy	Index	Area (px)	x	y	R.A. (deg)	Decl. (deg)	magF (mag)	magF_{err} (mag)	magN (mag)	magN_{err} (mag)	F_N (mag)	F_N_{err} (mag)	A_V (mag)	$\text{magF}_{\text{corr}}$ (mag)	$\text{magN}_{\text{corr}}$ (mag)	F_N_{corr} (mag)	Age (Myr)	Age_{err} (Myr)
(1)	(2)	(3)	(4)	(5)	(6)	(7)	(8)	(9)	(10)	(11)	(12)	(13)	(14)	(15)	(16)	(17)	(18)	(19)
N0253	9	50	717.97	235.69	12.0008408	−25.1647814	21.02	0.05	22.70	0.07	−1.67	0.09	0.44	19.75	21.49	−1.73	1	3.68
N0300	19489	51	1222.98	1490.43	13.8064014	−37.6938989	17.56	0.01	18.06	0.00	−0.49	0.01	0.16	17.03	17.56	−0.53	1	0.65
N0628	52	34	1691.48	1044.44	24.1500971	15.8364181	22.35	0.13	22.79	0.24	−0.43	0.27	0.69	20.05	20.93	−0.87	1	8.44
N1512	16	15	1025.59	205.14	61.0349597	−43.2103999	22.76	0.15	23.38	0.11	−0.61	0.19	0.47	21.44	22.11	−0.67	1	7.58
N1566	3479	12	687.39	909.39	65.0444367	−54.9389384	22.40	0.14	22.81	0.17	−0.40	0.22	0.52	20.90	21.66	−0.72	1	6.67
N2403	6770	46	2267.05	1658.14	114.0823638	65.6190926	16.68	0.01	17.37	0.00	−0.68	0.01	0.25	15.70	16.47	−0.75	1	0.60
N2903	4831	44	1063.66	1398.08	143.0592276	21.4778557	22.68	0.16	22.69	0.17	−0.01	0.23	0.98	19.80	20.44	−0.62	1.45	6.82
N3486	394	26	893.93	565.56	165.0738159	28.9906197	22.28	0.17	22.83	0.21	−0.55	0.27	0.30	21.30	22.07	−0.75	1	9.55
N4228	27	73	755.57	267.70	183.9339123	36.4000494	21.11	0.05	21.82	0.24	−0.70	0.25	0.11	20.60	21.25	−0.62	1	13.08
N4236	713	16	1290.46	1367.40	184.0784856	69.5126831	21.94	0.10	22.21	0.11	−0.26	0.15	0.88	19.50	20.26	−0.80	1	5.44
N4395	10880	12	957.91	1570.63	186.4872514	33.5039902	21.37	0.03	21.84	0.15	−0.47	0.16	0.14	20.90	21.44	−0.58	2.38	5.63
N5033	479	20	811.16	667.41	198.3917000	36.6324485	22.59	0.16	23.13	0.21	−0.54	0.26	0.29	21.70	22.44	−0.73	1	7.74
N5194	1654	49	838.21	961.66	202.5311662	47.2227261	21.98	0.15	21.57	0.17	0.41	0.23	1.54	17.60	18.11	−0.53	2.19	6.69
N5457	14264	88	2902.07	3032.20	210.7585709	54.2370707	20.76	0.06	20.75	0.065	0.01	0.09	1.22	17.4	18.11	−0.70	1	2.68
N7793	12718	425	1034.33	1224.31	359.4528215	−32.6170667	16.37	0.01	16.67	0.01	−0.29	0.01	0.09	16.0	16.30	−0.32	2.83	0.68
Holmber II	99	42	724.36	343.48	124.7976815	70.7728837	22.86	0.08	23.38	0.08	−0.51	0.12	0.046	22.52	23.06	−0.53	1	5.57
WLM	112	37	502.41	530.94	0.5160534	−15.3949499	22.73	0.09	23.27	0.18	−0.54	0.20	0.07	22.30	22.90	−0.64	2.14	7.74

Note. (1) Galaxy name, (2) index, (3) area (in pixel units, where 1 px = 0.″416 for UVIT), (4) x-coordinate in the UVIT image, (5) y-coordinate in the UVIT image, (6) R.A., (7) decl., (8) observed FUV magnitude, (9) FUV magnitude error, (10) observed NUV magnitude, (11) NUV magnitude error, (12) observed FUV−NUV color, (13) FUV−NUV color error, (14) A_V value corresponding to the SFC derived using the MB16 method (refer to Section 3.4), (15) attenuation-corrected FUV magnitude, (16) attenuation-corrected NUV magnitude, (17) attenuation-corrected FUV−NUV color, (18) derived age, and the (19) associated age error for each SFC respectively, in our catalog of ∼25,000 SFCs characterized in our 17 galaxies. We present the properties of the first SFC for each of our 17 galaxies in this table.

(This table is available in its entirety in machine-readable form in the online article.)

Appendix D
Radius Distribution of the SFCs

Figure 14 presents the radius distribution of the characterized SFCs in our 17 galaxies.

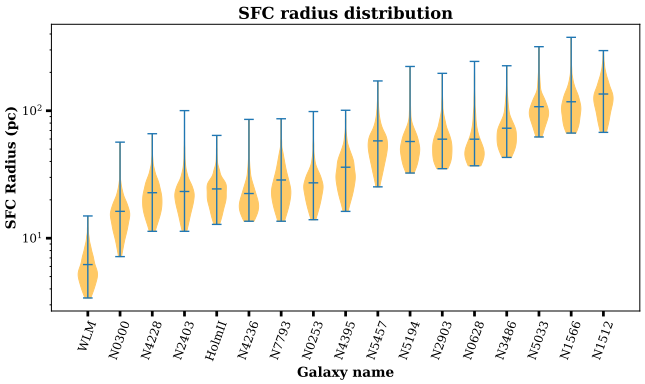


Figure 14. Violin plots for the radius distribution of the observed SFCs in all 17 galaxies, arranged in the increasing order of their distances. The central, top, and bottom bars represent the median, maximum and minimum SFC radius values for the galaxy, respectively. As expected, we detect larger SFC in galaxies that are located further away and vice versa.

Appendix E
A_V Maps of Galaxies at the SFC Positions

In Figure 15, we present the A_V maps corresponding to the positions of the characterized SFCs within our galaxies. The full A_V tables with much larger coverage (see Table 7) used to create these dust attenuation maps with 6″ resolution rectangular grids can be accessed online.

Table 7
The A_V Tables Used to Create the Dust Attenuation Maps Used in This Paper

Galaxy (1)	Index (2)	R.A. (3)	Decl. (4)	k_{24} μm (5)	A_V (6)
N0253	2	11.7047086	−25.4197496	3.91	0.25

Note. (1) Galaxy name, (2) index of the 6″ rectangular grid, (3) R.A., (4) decl., (5) k_{24_μ} value (refer to Section 3.4), and (6) A_V value measured for each particular bin.

(This table is available in its entirety in machine-readable form in the online article.)

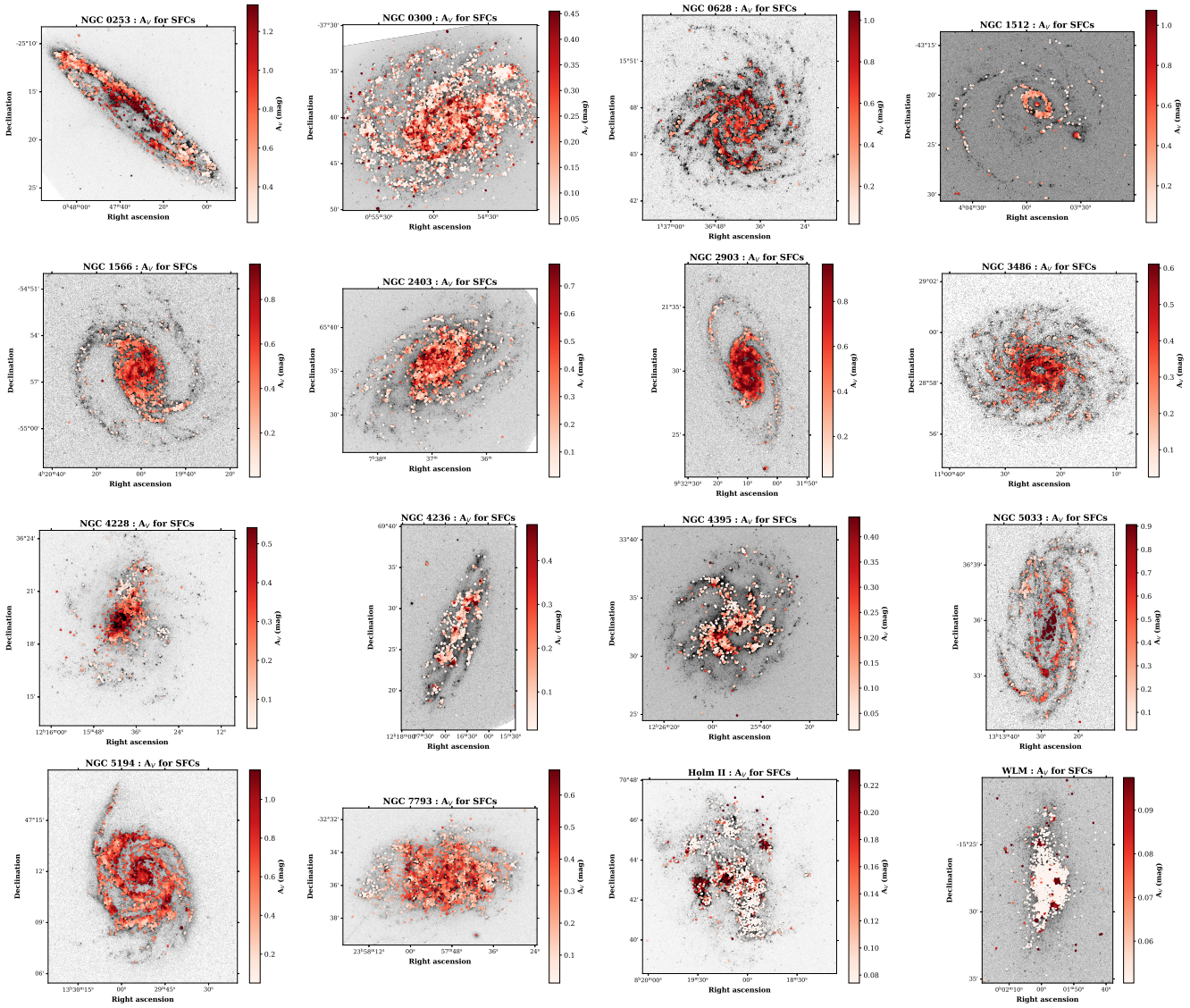


Figure 15. A_V maps of the 16 out of 17 galaxies at the SFC positions, barring NGC 5457, for which see Figure 3.

Appendix F
Mathematical Expressions Used for Dust Attenuation Correction

1. The conversion of FUV and NUV source counts into the AB magnitude and the spectral flux units is performed according to the calibrations provided in S. N. Tandon et al. (2017, 2020).
2. 2MASS *J*-band magnitudes are defined in the Vega system and need to be converted to AB magnitude system in our analysis; In the *J*-band fits files accessed from NED, pixel values are written in counts:

$$\begin{aligned} \mathrm{mag}J_{AB} &= \mathrm{mag}J_{\mathrm{Vega}} + 0.91 \\ &= ZP_J + 2.5 * \log_{10}(\mathrm{counts}_J) + 0.91. \end{aligned} \quad \text{(F1)}$$

3. In the process of A_{FUV} estimation, MIPS 24 μm and FUV luminosities are used. The pixel values of MIPS 24 μm fits files taken from NED are written in MJy sr^{-1}. The FUV fits files are written in source counts. The conversion of both these data between mJy and erg s^{-1} is achieved as follows:

$$\mathrm{FUV(in\ mJy)} = k_1 * \mathrm{cps}_{\mathrm{FUV}}. \quad \text{(F2)}$$

Here, k_1 = 0.227 for F148W, 0.282 for F154W, and 0.419 for F169M filter (derived using the S. N. Tandon et al. (2017) calibrations), and thus

$$24\mu\mathrm{(in\ mJy)} = 0.529 * \mathrm{counts}_{24\mu}. \quad \text{(F3)}$$

Finally, the conversion of FUV and 24 μm spectral energy densities into luminosity units and their subsequent use in the derivation of A_{FUV} is performed as

$$A_{\mathrm{FUV}} = 2.5 * \log_{10}\left[1 + \frac{k_i * 24\mu\ (\mathrm{mJy})}{\mathrm{ratio} * \mathrm{FUV(mJy)}}\right], \quad \text{(F4)}$$

where k_i equals the M. Boquien et al. (2016) equivalent factor for the C.-N. Hao et al. (2011) 3.89 values. The ratio here is equal to 162 for F148W, 156 for F154W, and 142 for F169M filter, and is simply the ratio of central wavelength of MIPS 24 μm and the respective FUV filter.

Appendix G
Effect of Variation in A_V within a 6″ Resolution Element on SFC Ages

To quantify the variation in A_V within a resolution element owing to the mismatch in the angular resolution of our attenuation maps (6″) and the UVIT's detection scale (1.″5), we selected NGC 0628 as our test case. NGC 0628 is the nearest galaxy for which MUSE-based A_V maps at ∼0.″92 resolution (F. Santoro et al. 2022) are available, and it is assumed that the MUSE-based A_V maps have comparable resolution to the UVIT's (1.″5).

We have 882 SFCs in the full disk of NGC 0628, out of which ∼450 SFCs lie within the MUSE-covered area of the galaxy. Approximately 2200 H II regions have been identified in this area of NGC 0628 by F. Santoro et al. (2022). First, we crossmatched the SFC positions with our A_V map and identified 148 6″ bins in which more than one SFC is present. In total, 367 SFCs are located within these 148 6″ bins. Next, we crossmatched these 367 SFC positions with the MUSE H II regions and measured the higher-resolution MUSE-based A_V values.

This allows us to measure the A_V variation within a resolution element, using the 367 SFCs as probes. First, we observed that our A_V values and MUSE-based A_V values span a similar distribution with comparable median values (see Figure 16). However, it is noteworthy that MUSE-based A_V measurements include extreme values at both the lower end (close to 0) and the upper end (between 1.20 and 1.80) of A_V. Owing to our coarser 6″ resolution, such values are missing in our A_V maps and are likely smoothed out (similar to the histograms presented in Figure 6 and 7). The A_V difference histogram roughly spans between −1.0 and +1.0 magnitude, with over 85% values lying between −0.5 and 0.5 magnitude. The A_V difference median is −0.04 mag and standard deviation is ±0.18 mag.

In order to understand how the resolution-dependent A_V variation affects the SFC ages, we corrected these 367 SFCs using our A_V values (used in this paper) and MUSE-based A_V values. The UV CMD thus created indicates small variations in the FUV–NUV color. However, this variation is not systematic toward either bluer or redder colors. Next, we created an age-difference map and histogram for the SFCs, after correcting these with our A_V values and MUSE-based A_V values. Approximately 60% of the SFCs exhibit age variations within 30 Myr, whereas the median and standard deviation of the age-difference distribution is measured to be 1 Myr and ±28 Myr. These age differences are largely within the magnitude error,

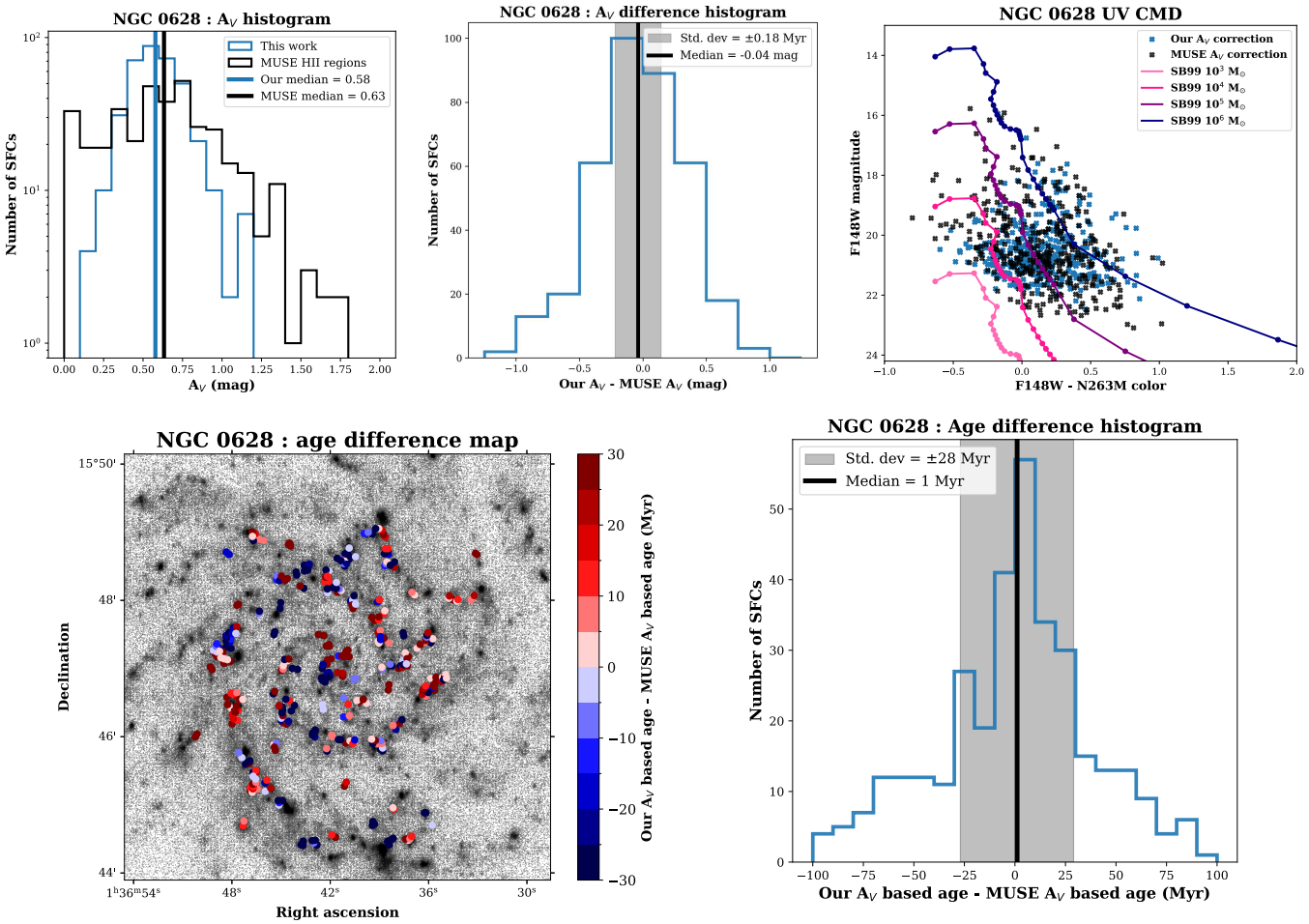


Figure 16. Top left: histogram of our 6″ resolution A_V values and MUSE-based A_V values for the MUSE-covered region of NGC 0628. MUSE-based A_V values span a slightly wider range, whereas the extreme values at both the lower and upper end of A_V are likely smoothed out in our A_V maps. Top middle: A_V difference histogram showing that over 85% of the difference values lie between −0.5 and 0.5 mag. Top right: UV CMD for the 367 SFCs in NGC 0628 after correcting them using our A_V values and MUSE-based A_V values. The spatial age-difference map (bottom left) and the age-difference histogram (bottom right) for these SFCs reveal that most of the age differences lie between ±30 Myr, which is within the associated SFC age errors.

and the corresponding age errors associated with the SFCs. This analysis allows us to conclude that the resolution mismatch between the UVIT and our own A_V map leads to no systematic shifts in the SFC ages. Using a higher-resolution A_V map may lead to more accurate dust attenuation; however, its impact on the derived ages and the overall age demographics may not be particularly significant.

Appendix H
Effect of Variable Spatial Resolution across the Galaxy Sample on the Age Demographic

In order to establish that our age trends are not driven by the variation in physical resolution across our galaxy sample (between 6 and 137 pc), we tested the robustness of our age demographics and gradients. We chose NGC 7793 and NGC 2403 for this test due to their proximity, large exposure times, and an abundance of SFCs with better than 10σ detection (i.e., 0.10 mag error cut). The UVIT resolution corresponds to a native physical scale of ∼19–24 pc for these galaxies. We degraded the galaxy images to 50 and 100 pc resolution and characterized the SFCs with less than 0.10 mag error (equivalent to 10σ detection) at these resolution values. We then compared the native resolution, 50 and 100 pc resolution age maps and radial gradients. The visual inspection of age maps (see Figure 17) reveals a reasonable match in the location of young and old SFCs within galaxies. In terms of absolute ages, it can be observed that poorer-resolution images lead to systematically older SFC ages, which is further supported by the observed age gradients. (The gradient shifts upward on the y-axis as poorer-resolution images are used) This happens due to the contamination caused by underlying older disk stars, as the SFC flux is integrated over a larger area (D. Calzetti et al. 2025). However, the negative slope and shape of the gradient are mostly preserved, considering the age uncertainties (∼23 Myr for 0.10 mag error) associated with our SFCs.

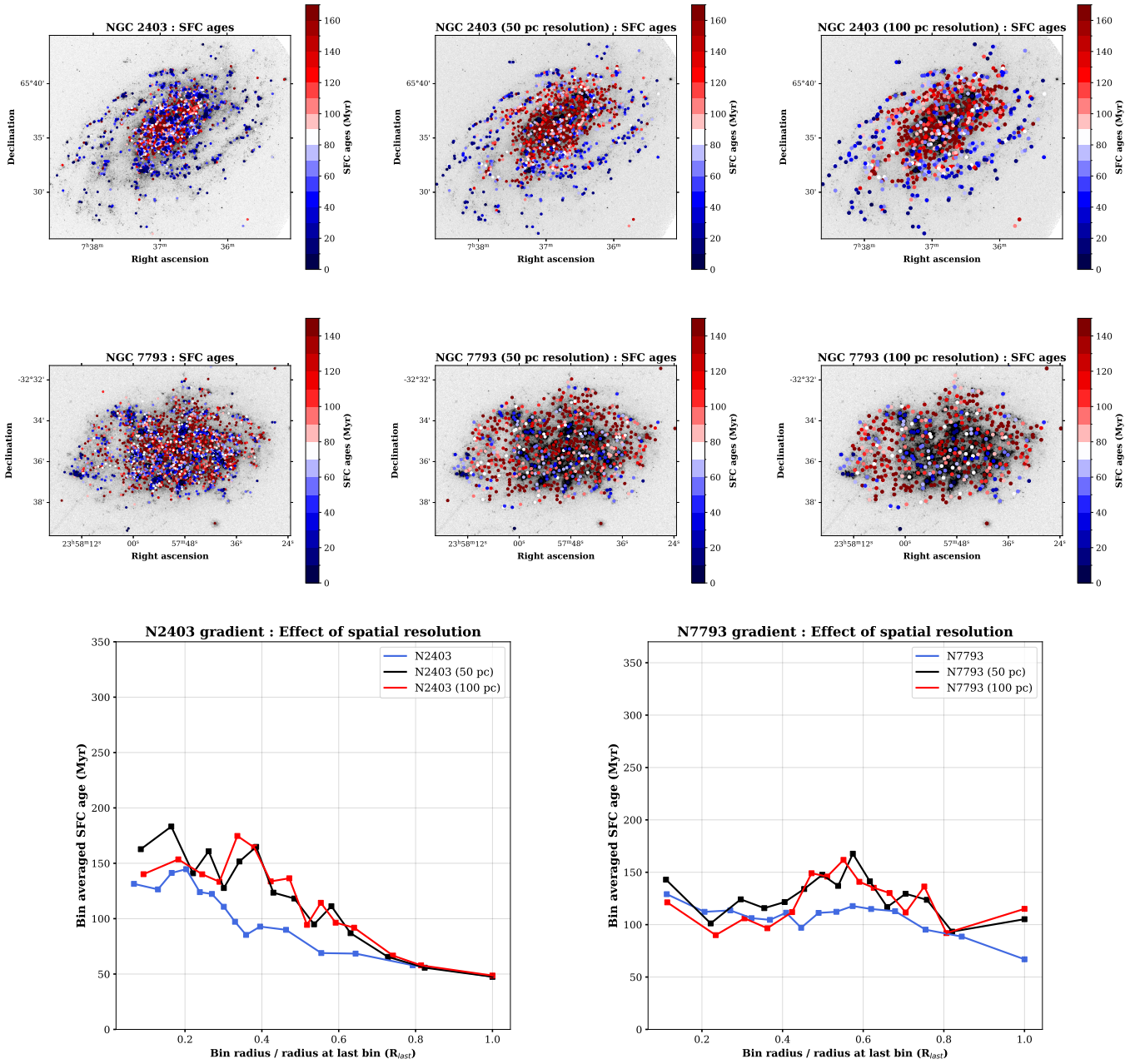


Figure 17. Top and middle rows, from left to right, show spatial age maps of SFCs with <0.10 mag error cuts in NGC 2403 (top row) and NGC 7793 (middle row), created at native resolution (same as Figures 10 and 11), 50 pc resolution, and 100 pc resolution. A reasonable match in the location of young and old SFCs within the galaxies is observed. The bottom row shows radial SFC age gradients in NGC 2403 (left) and NGC 7793 (right), measured using the native resolution (blue points), 50 pc resolution (black points), and 100 pc resolution (red points) SFC age maps. The negative slopes and shapes of the gradients are mostly preserved, irrespective of the spatial resolution.

ORCID iDs

Gairola Shashank https://orcid.org/0009-0008-1250-6128
Smitha Subramanian https://orcid.org/0000-0002-5331-6098
Chayan Mondal https://orcid.org/0000-0003-4531-0945
Shyam H. Menon https://orcid.org/0000-0001-5944-291X
Annapurni Subramaniam https://orcid.org/0000-0003-4612-620X

References

Adamo, A., Ryon, J. E., Messa, M., et al. 2017, ApJ, 841, 131
Agrawal, P. C. 2006, AdSpR, 38, 2989
Akhil, K. R., Kartha, S. S., Krishnan, U., et al. 2025, PASA, 42, e056
Amrutha, S., Das, M., & Yadav, J. 2024, MNRAS, 530, 2199
Ananthu, S., Shashank, G., Subramanian, S., et al. 2026, ApJ, 1002, 220
Astropy Collaboration, Price-Whelan, A. M., Sipőcz, B. M., et al. 2018, AJ, 156, 123
Barnes, K. L., van Zee, L., & Skillman, E. D. 2011, ApJ, 743, 137
Bianchi, L., Thilker, D. A., Burgarella, D., et al. 2005, ApJ, 619, L71
Boquien, M., Burgarella, D., Roehlly, Y., et al. 2019, A&A, 622, A103
Boquien, M., Kennicutt, R., Calzetti, D., et al. 2016, A&A, 591, A6
Bradley, L., Sipőcz, B., Robitaille, T., et al. 2024, astropy/photutils: v1.12.0, Zenodo, doi:10.5281/zenodo.10967176
Bresolin, F. 2019, MNRAS, 488, 3826
Buat, V., Iglesias-Páramo, J., Seibert, M., et al. 2005, ApJ, 619, L51
Burgarella, D., Buat, V., & Iglesias-Páramo, J. 2005, MNRAS, 360, 1413
Buta, R. J., Corwin, H. G., & Odewahn, S. C. 2007, The de Vaucouleurs Atlas of Galaxies (Cambridge Univ. Press)
Calzetti, D., Kennicutt, R. C., Engelbracht, C. W., et al. 2007, ApJ, 666, 870
Calzetti, D., Lee, J. C., Sabbi, E., et al. 2015, AJ, 149, 51

Calzetti, D., Kennicutt, R. C., Adamo, A., et al. 2025, ApJ, 991, 198
Calzetti, D., Kennicutt, R. C., Adamo, A., et al. 2025, ApJ, 991, 198
Cardelli, J. A., Clayton, G. C., & Mathis, J. S. 1989, ApJ, 345, 245
Chauhan, R., Subramanian, S., Kudari, D. A., Amrutha, S., & Das, M. 2025, A&A, 702, A222
Chyży, K. T., Bomans, D. J., Krause, M., et al. 2007, A&A, 462, 933
Cook, D. O., Lee, J. C., Adamo, A., et al. 2019, MNRAS, 484, 4897
Cortese, L., Boselli, A., Franzetti, P., et al. 2008, MNRAS, 386, 1157
Côté, P., Woods, T., Hutchings, J. B., et al. 2025, JATIS, 11, 042202
Dale, D. A., Smith, J. D. T., Schlawin, E. A., et al. 2009, ApJ, 693, 1821
Davidge, T. J. 2010, ApJ, 725, 1342
de Vaucouleurs, G., de Vaucouleurs, A., Corwin, H. G., Jr., et al. 1991, Third Reference Catalogue of Bright Galaxies (Springer)
Della Bruna, L., Adamo, A., Lee, J. C., et al. 2021, A&A, 650, A103
Devaraj, A., Joseph, P., Stalin, C. S., Tandon, S. N., & Ghosh, S. K. 2023, ApJ, 946, 65
Elmegreen, B. G., Elmegreen, D. M., Chandar, R., Whitmore, B., & Regan, M. 2006, ApJ, 644, 879
Elmegreen, D. M., & Elmegreen, B. G. 2014, ApJ, 781, 11
Elmegreen, D. M., Elmegreen, B. G., Adamo, A., et al. 2014, ApJL, 787, L15
Emsellem, E., Schinnerer, E., Santoro, F., et al. 2022, A&A, 659, A191
Fathi, K., Izumi, T., Romeo, A. B., et al. 2015, ApJL, 806, L34
García-Benito, R., González Delgado, R. M., Pérez, E., et al. 2017, A&A, 608, A27
George, K., Poggianti, B. M., Gullieuszik, M., et al. 2018, MNRAS, 479, 4126
Gil de Paz, A., Boissier, S., Madore, B. F., et al. 2007, ApJS, 173, 185
Gogarten, S. M., Dalcanton, J. J., Williams, B. F., et al. 2010, ApJ, 712, 858
Gouliermis, D. A. 2018, PASP, 130, 072001
Grasha, K., Calzetti, D., Adamo, A., et al. 2017, ApJ, 840, 113
Grasha, K., Calzetti, D., Bittle, L., et al. 2018, MNRAS, 481, 1016
Graus, A. S., Bullock, J. S., Fitts, A., et al. 2019, MNRAS, 490, 1186
Groves, B., Kreckel, K., Santoro, F., et al. 2023, MNRAS, 520, 4902
Hao, C.-N., Kennicutt, R. C., Johnson, B. D., et al. 2011, ApJ, 741, 124
Harris, C. R., Millman, K. J., van der Walt, S. J., et al. 2020, Natur, 585, 357
Hassani, H., Rosolowsky, E., Koch, E. W., et al. 2024, ApJS, 271, 2
Ho, S. H., Martin, C. L., & Turner, M. L. 2019, ApJ, 875, 54
Hota, S., Subramaniam, A., Dhanush, S. R., Cioni, M.-R. L., & Subramanian, S. 2024a, MNRAS, 532, 322
Hota, S., Subramaniam, A., Nayak, P. K., & Subramanian, S. 2024b, AJ, 168, 255
Hubble, E. P. 1936, Realm of the Nebulae (Yale Univ. Press)
Hunt, L. K., De Looze, I., Boquien, M., et al. 2019, A&A, 621, A51
Hunter, J. D. 2007, CSE, 9, 90
Iglesias-Paramo, J., Boselli, A., Gavazzi, G., & Zaccardo, A. 2004, A&A, 421, 887
Jarrett, T. H., Chester, T., Cutri, R., Schneider, S. E., & Huchra, J. P. 2003, AJ, 125, 525
Kennicutt, R. C., Jr., Armus, L., Bendo, G., et al. 2003, PASP, 115, 928
Keshri, S., Barway, S., Das, M., Yadav, J., & Combes, F. 2025, A&A, 695, A39
Kim, D., Jansen, R. A., Windhorst, R. A., Cohen, S. H., & McCabe, T. J. 2019, ApJ, 884, 21
Kormendy, J. 2013, in Secular Evolution of Galaxies, ed. J. Falcón-Barroso & J. H. Knapen (Cambridge Univ. Press)
Kormendy, J., & Kennicutt, R. C., Jr. 2004, ARA&A, 42, 603
Koyama, Y., Shimakawa, R., Yamamura, I., Kodama, T., & Hayashi, M. 2019, PASJ, 71, 8
Kreckel, K., Groves, B., Schinnerer, E., et al. 2013, ApJ, 771, 62
Kroupa, P. 2001, MNRAS, 322, 231
Krumholz, M. R., McKee, C. F., & Bland-Hawthorn, J. 2019, ARA&A, 57, 227
Kumar, A., Ghosh, S. K., Hutchings, J., et al. 2012, SPIE, 8443, 84431N
Larson, R. B. 1976, MNRAS, 176, 31
Leahy, D. A., Postma, J., Chen, Y., & Buick, M. 2020, ApJS, 247, 47
Lee, J. C., Whitmore, B. C., Thilker, D. A., et al. 2022, ApJS, 258, 10
Leitherer, C., Schaerer, D., Goldader, J. D., et al. 1999, ApJS, 123, 3
Lemonias, J. J., Schiminovich, D., Thilker, D., et al. 2011, ApJ, 733, 74
Leroy, A. K., Walter, F., Brinks, E., et al. 2008, AJ, 136, 2782
Leroy, A. K., Schinnerer, E., Hughes, A., et al. 2021, ApJS, 257, 43
Levesque, E. M., & Leitherer, C. 2013, ApJ, 779, 170
Lin, C. C., & Shu, F. H. 1964, ApJ, 140, 646
Linden, S. T., Perez, G., Calzetti, D., et al. 2022, ApJ, 935, 166
Liu, G., Koda, J., Calzetti, D., Fukuhara, M., & Momose, R. 2011, ApJ, 735, 63
Maschmann, D., Lee, J. C., Thilker, D. A., et al. 2024, ApJS, 273, 14
Meena, B., Sabbi, E., Zeidler, P., et al. 2025, ApJ, 987, 33
Menon, S. H., Grasha, K., Elmegreen, B. G., et al. 2021, MNRAS, 507, 5542
Mo, H. J., Mao, S., & White, S. D. M. 1998, MNRAS, 295, 319
Mondal, C., Subramaniam, A., & George, K. 2018, AJ, 156, 109
Mondal, C., Subramaniam, A., George, K., et al. 2021, ApJ, 909, 203
Muñoz-Mateos, J. C., Gil de Paz, A., Boissier, S., et al. 2007, ApJ, 658, 1006
Naab, T., & Ostriker, J. P. 2006, MNRAS, 366, 899
Nandi, P., Stalin, C. S., Saikia, D. J., et al. 2023, ApJ, 950, 81
Parikh, T., Thomas, D., Maraston, C., et al. 2021, MNRAS, 502, 5508
Pasquali, A., Leroy, A., Rix, H.-W., et al. 2008, ApJ, 687, 1004
Pedregosa, F., Varoquaux, G., Gramfort, A., et al. 2011, JMLR, 12, 2825
Postma, J. E., & Leahy, D. 2017, PASP, 129, 115002
Qin, J., Zheng, X. Z., Wuyts, S., Pan, Z., & Ren, J. 2019, ApJ, 886, 28
Radburn-Smith, D. J., Roškar, R., Debattista, V. P., et al. 2012, ApJ, 753, 138
Rakhi, R., Santhosh, G., Joseph, P., et al. 2023, MNRAS, 522, 1196
Riggs, C. L., Brooks, A. M., Munshi, F., et al. 2024, ApJ, 977, 20
Rodríguez, M. J., Baume, G., & Feinstein, C. 2020, A&A, 644, A101
Romeo, A. B., & Falstad, N. 2013, MNRAS, 433, 1389
Romeo, A. B., & Fathi, K. 2016, MNRAS, 460, 2360
Romeo, A. B., & Mogotsi, K. M. 2017, MNRAS, 469, 286
Rosolowsky, E. W., Pineda, J. E., Kauffmann, J., & Goodman, A. A. 2008, ApJ, 679, 1338
Sabbi, E., Meena, B., Zeidler, P., et al. 2026, ApJ, 1000, 241
Sacchi, E., Cignoni, M., Aloisi, A., et al. 2019, ApJ, 878, 1
Salim, S., Rich, R. M., Charlot, S., et al. 2007, ApJS, 173, 267
Santhosh, G., Rajalakshmi, R., George, K., Subramanian, S., & Indulekha, K. 2025, PASA, 42, e073
Santoro, F., Kreckel, K., Belfiore, F., et al. 2022, A&A, 658, A188
Sauvage, M., & Thuan, T. X. 1992, ApJL, 396, L69
Schlafly, E. F., & Finkbeiner, D. P. 2011, ApJ, 737, 103
Shabani, F., Grebel, E. K., Pasquali, A., et al. 2018, MNRAS, 478, 3590
Shashank, G., Subramanian, S., Muraleedharan, S., et al. 2025, A&A, 693, A188
Singh, K. P., Tandon, S. N., Agrawal, P. C., et al. 2014, SPIE, 9144, 91441S
Smith, M. V., van Zee, L., Dale, D. A., et al. 2022, MNRAS, 515, 3270
Subramaniam, A. 2022, JApA, 43, 80
Subramanian, S., Mondal, C., & Kalari, V. 2024, A&A, 681, A8
Tandon, S. N., Subramaniam, A., Girish, V., et al. 2017, AJ, 154, 128
Tandon, S. N., Postma, J., Joseph, P., et al. 2020, AJ, 159, 158
Thean, A. H. C., Mundell, C. G., Pedlar, A., & Nicholson, R. A. 1997, MNRAS, 290, 15
Thilker, D. A., Bianchi, L., Boissier, S., et al. 2005a, ApJL, 619, L79
Thilker, D. A., Hoopes, C. G., Bianchi, L., et al. 2005b, ApJL, 619, L67
Thilker, D. A., Bianchi, L., Meurer, G., et al. 2007, ApJS, 173, 538
Thilker, D. A., Lee, J. C., Whitmore, B. C., et al. 2025, ApJS, 280, 1
Tremonti, C. A., Heckman, T. M., Kauffmann, G., et al. 2004, ApJ, 613, 898
Turner, J. A., Dale, D. A., Lee, J. C., et al. 2021, MNRAS, 502, 1366
Ujjwal, K., Kartha, S. S., Subramanian, S., et al. 2022, MNRAS, 516, 2171
Van Rossum, G., & Drake, F. L. 2009, Python 3 Reference Manual (CreateSpace)
VanderPlas, J., Connolly, A. J., Ivezic, Z., & Gray, A. 2012, in Proc. of the Conference on Intelligent Data Understanding (CIDU) (IEEE), 47
Virtanen, P., Gommers, R., Oliphant, T. E., et al. 2020, NaMet, 17, 261
Watts, C., Das, M., & Barway, S. 2024, ApJ, 974, 206
White, S. D. M., & Frenk, C. S. 1991, ApJ, 379, 52
Williamson, D., Martel, H., & Romeo, A. B. 2016, ApJ, 831, 1
Yadav, J., Das, M., Patra, N. N., et al. 2021, ApJ, 914, 54
Zheng, Y., Putman, M. E., Emerick, A., et al. 2019, MNRAS, 490, 467
Zhou, Z.-M., Cao, C., & Wu, H. 2015, AJ, 149, 1